U.S. DEPARTMENT OF ENERGY | Office of Science

Doppler Lidar (DL) Instrument Handbook

RK Newsom   R Krishnamurthy

December 2022

ARM

DISCLAIMER

Doppler Lidar (DL) Instrument Handbook

RK Newsom
R Krishnamurthy
Both at Pacific Northwest National Laboratory

December 2022

How to cite this document:

Acronyms and Abbreviations

ACF	autocovariance function
ADC	ARM Data Center
AET	After Effects Project Template (by Adobe Systems Incorporated)
AGL	above ground level
AMF	ARM Mobile Facility
ARM	Atmospheric Radiation Measurement
ASI	Ascension Island
AWAKEN	American Wake Experiment
CACTI	Cloud, Aerosol, and Complex Terrain Interactions
COMBLE	Cold-Air Outbreaks in the Marine Boundary Layer Experiment
COR	Córdoba, Argentina
DL	Doppler lidar
DLWSTATS	Doppler Lidar Vertical Velocity Statistics Value-Added Product
ENA	Eastern North Atlantic
FFT	fast Fourier transform
GIF	Guest Instrument Facility
GoAmazon	Green Ocean Amazon 2014/15
GPS	Global Positioning System
GVAX	Ganges Valley Aerosol Experiment
I&Q	in-phase and quadrature signals
IMU	inertial measurement unit
IOP	intensive operational period
IR	infrared
LASIC	Layered Atlantic Smoke Interactions with Clouds
LO	local oscillator
MAO	Manacapuru, Brazil
MOPA	master oscillator power amplifier
MOSAiC	Multidisciplinary Drifting Observatory for the Study of Arctic Climate
MSL	mean sea level
MUR	maximum unambiguous range
NAV	Navigational Location and Attitude
netCDF	Network Common Data Form
NSA	North Slope of Alaska
OLI	Oliktok Point
PECAN	Plains Elevated Convection at Night

PPI	plan position indicator
PRF	pulse repetition frequency
PSU	power supply unit
RCF	Radiometer Calibration Facility
RHI	range height indicator
RL	Raman lidar
SAIL	Surface Atmosphere Integrated Field Laboratory
SGP	Southern Great Plains
SNR	signal-to-noise ratio
TBD	To be determined
TCAP	Two-Column Aerosol Project
TKE	total kinetic energy
TRACER	Tracking Aerosol Convection Interactions Experiment
TWP	Tropical Western Pacific
UTC	Coordinated Universal Time
VAP	value-added product
XPIA	eXperimental Planetary boundary layer Instrumentation Assessment

Contents

Figures

Tables

1.0   General Overview

The Doppler lidar (DL) is an active remote-sensing instrument that provides range- and time-resolved measurements of radial velocity, attenuated backscatter, and signal-to-noise ratio (SNR). The principle of operation is similar to radar in that pulses of electromagnetic energy (infrared in this case) are transmitted into the atmosphere; the energy scattered back to the transceiver is collected and measured as a time-resolved signal. From the time delay between each outgoing transmitted pulse and the backscattered signal, the distance to the scatterer is inferred. The radial or line-of-sight velocity of the scatterers is determined from the Doppler frequency shift of the backscattered radiation. The DL uses a heterodyne detection technique in which the return signal is mixed with a reference laser beam (i.e., local oscillator) of known frequency. An onboard signal-processing computer then determines the Doppler frequency shift from the power spectra of the heterodyne signal. The energy content of the Doppler spectra can also be used to estimate attenuated backscatter.

The DL operates in the near-infrared (IR;1.5 microns) and is sensitive to backscatter from micron-sized aerosols. Aerosols are ubiquitous in the lower troposphere and behave as ideal tracers of atmospheric winds. In contrast to radar, the DL is capable of measuring radial velocities under clear-sky conditions with very good precision (typically ~10 cm/sec). Also, most of the U.S. Department of Energy Atmospheric Radiation Measurement (ARM) user facility DLs have full upper-hemispheric scanning capability, enabling three-dimensional mapping of turbulent flows in the atmospheric boundary layer. When the scanner is pointed vertically the DL provides height- and time-resolved measurements of vertical velocity. Radial velocities are defined to be positive for motion away from the lidar.

The DL is a small self-contained system that is easily portable and has relatively modest power requirements. The instrument is housed in a rugged environmentally controlled container, requires only external electrical power and internet, and will run unattended for weeks or months on end with little or no operator intervention. Control of the system is facilitated through either a direct connection to the onboard instrument computer or remotely via the internet. The control software enables the user to easily modify a variety of instrument settings and schedule a variety of different scans.

Researchers who are considering use of ARM resources should consider how the existing suite of Doppler lidars might be used to address their science questions. Researchers should therefore be aware that the lidars can be configured in a number of different ways, and that the current operational configuration can be modified for specific intensive operational periods (IOPs). Specifically, researchers should consider how different scan strategies might be used to address their research goals.

2.0   Contacts

2.1   ARM Instrument Mentors

Rob Newsom
Pacific Northwest National Laboratory
902 Battelle Boulevard
P.O. Box 999, MSIN K9-30

Richland, Washington 99352
Phone: 509-372-6020
Fax: 509-372-6168
email: rob.newsom@pnl.gov

Raghavendra Krishnamurthy
Pacific Northwest National Laboratory
902 Battelle Boulevard
P.O. Box 999, MSIN K9-24
Richland, Washington 99352
Phone: 509-375-7310
email: raghavendra.krishnamurthy@pnnl.gov

2.2   Instrument Developer

Halo Photonics
Unit 2, Bank Farm
Brockamin, Leigh, Worcestershire
United Kingdom WR6 5LA GB
Phone: +44 (0) 1886 833489
Web site: www.halo-photonics.com
Guy Pearson: guy@halo-photonics.com
Justin Eacock: jus@halo-photonics.com

3.0   Deployment Locations and History

As of the beginning of 2023, the ARM facility operates 15 coherent Doppler lidar systems at various sites around the world. To date, these systems have primarily been used to make high-resolution measurements of vertical velocity, attenuated backscatter, and horizontal winds in the atmospheric boundary layer.

ARM acquired its first three Doppler lidars in 2010 from Halo Photonics. Additional systems were acquired from Halo Photonics in 2014, 2016, 2019, 2020, 2021, and 2022. Table 1 lists the current ARM Doppler lidar inventory by vendor, model, serial number, and year acquired.

Table 1.   ARM Doppler lidars listed by vendor, model, serial number, and year acquired by ARM. Also listed is the pulse repetition frequency (PRF) for each system.

Vendor	Model	Serial number	PRF (kHz)	Year acquired
Halo Photonics	Stream Line	0910-07	15	2010
Halo Photonics	Stream Line	0910-08	15	2010
Halo Photonics	Stream Line	0910-09	15	2010
Halo Photonics	Stream Line Pro	0514-82	15	2014
Halo Photonics	Stream Line	0514-83	15	2014
Halo Photonics	Stream Line	0514-84	15	2014

Vendor	Model	Serial number	PRF (kHz)	Year acquired
Halo Photonics	XR	0116-107	10	2016
Halo Photonics	Stream Line	0116-108	15	2016
Halo Photonics	Stream Line Pro	0116-109	15	2016
Halo Photonics	Stream Line Pro	0319-160	15	2019
Halo Photonics	XR+	0720-193	10	2020
Halo Photonics	XR+	0921-214	10	2021
Halo Photonics	XR+	0921-215	10	2021
Halo Photonics	XR+	0322-236	10	2022
Halo Photonics	XR+	0322-237	10	2022

As indicated in Table 1, the current inventory of Doppler lidars includes four models of Halo Doppler lidars. The Stream Line, XR, and XR+ all incorporate many of the same design features, including an external scanner that permits the beam to be steered anywhere within the upper hemisphere, but the Stream Line XR and XR+ use enhanced signal processors and data acquisition cards, and transmit higher pulse energies compared to the standard Stream Line models. Also, the XR and XR+ models operate at pulse repetition frequencies (PRFs) of 10 kHz, whereas the Stream Line and Stream Line Pro models operate at 15 kHz.

The Stream Line Pro models use an internal scanner with a reduced field of regard that only permits the beam to be steered within 20° from zenith, for any azimuth angle. As such, the Stream Line Pro is used primarily for vertical profiling of winds and vertical velocity. The ARM Stream Line Pros also use a 50-mm aperture as opposed to the 75-mm aperture in the Stream Line and XR models. This enables the Stream Line Pro to have a shorter minimum range than the Stream Line or the XR. Section 6.2 discusses the performance specifications in greater detail.

Figure 1.   The Halo Photonics Stream Line Pro and Stream Line (left), XR (middle), and XR+ (right).

Tables 2 through 16 summarize the deployment history for each of the ARM Doppler lidar systems listed in Table 1.

Table 2.   Deployment history for 0910-07 (Stream Line).

Deployment dates		Location				
Start	End	Site-Facility	Latitude (deg North)	Longitude (deg East)	Altitude (m MSL)	Comment
20160503	Present	SGP E41	36.879945	-97.086387	340	Top of profiling module
20110421	20160502	SGP C1	36.605297	-97.48649	316	Next to 915MHz
20101015	20101201	SGP C1	36.60545	-97.48579	319	Deck behind GIF

Table 3.   Deployment history for 0910-08 (Stream Line).

Deployment dates		Location				
Start	End	Site-Facility	Latitude (deg North)	Longitude (deg East)	Altitude (m MSL)	Comment
20211117	20220123	SGP S01	36.605200	-97,485700	317	Dual mode @ C1
20160413	Present	SGP E39	36.819656	-97.819869	337	Top of profiling module
20150723	20160408	SGP S01	36.607765	-97.486988	312	Dual mode @ C1
20150601	20150715	n/a	mobile			PECAN offsite IOP
20150306	20150416	n/a	40.048794	-105.003853	1583	XPIA offsite IOP
20101206	20150104	TWP C3	-12.424547	130.89153	29.9	Top of D Van

Table 4.   Deployment history for 0910-09 (Stream Line).

Deployment dates		Location				
Start	End	Site-Facility	Latitude (deg North)	Longitude (deg East)	Altitude (m MSL)	Comment
20210825	20221001	HOU M1	29.669876	-95.0597	8	TRACER
20190825	20200320	ANX S2	74.503444	19.004528	15	COMBLE
20180923	20190430	COR M1	-32.12637	-64.72854	1141	CACTI
20160906	20171101	ASI M1	-7.9679	-14.35039	341	LASIC
20140101	20150828	MAO M1	-3.21321	-60.59829	53	GOAMAZON
20120701	20130619	PVC M1	42.03046	-70.04932	57	TCAP
20110621	20120331	PGH M1	29.358843	79.458228	1942	GVAX
20101015	20101130	SGP S01	36.60701	-97.48796	315	SGP C1 Near RCF

Table 5.   Deployment history for 0514-82 (Stream Line Pro).

Deployment dates		Location				
Start	End	Site-Facility	Latitude (deg North)	Longitude (deg East)	Altitude (m MSL)	Comment
20140801	Present	NSA C1	71.322947	-156.61609	8	Installed on Great White deck

Table 6.   Deployment history for 0514-83 (Stream Line).

Deployment dates		Location				
Start	End	Site-Facility	Latitude (deg North)	Longitude (deg East)	Altitude (m MSL)	Comment
20221109	present	S5	36.318198	-97.409079	322	AWAKEN site A2
20190419	20220927	SGP E32	36.819656	-97.819869	335	Top of trailer
20160524	20190419	SGP E37	36.310853	-97.9274278	389	Top of trailer
20140801	20160512	OLI M1	70.494856	-149.88647	6	Top of trailer

Table 7.   Deployment history for 0514-84 (Stream Line).

Deployment dates		Location				
Start	End	Site-Facility	Latitude (deg North)	Longitude (deg East)	Altitude (m MSL)	Comment
20141020	Present	ENA C1	39.091177	-28.026825	33	Top of trailer

Table 8.   Deployment history for 0116-107 (XR).

Deployment dates		Location				
Start	End	Site-Facility	Latitude (deg North)	Longitude (deg East)	Altitude (m MSL)	Comment
20160502	Present	SGP C1	36.605295	-97.486581	319	Top of RL utility van

Table 9.   Deployment history for 0116-108 (Stream Line).

Deployment dates		Location				
Start	End	Site-Facility	Latitude (deg North)	Longitude (deg East)	Altitude (m MSL)	Comment
20190419	Present	SGP E37	36.310853	-97.9274278	389	Top of trailer
20160503	20190419	SGP E32	36.819656	-97.819869	335	Top of trailer

Table 10.   Deployment history for 0116-109 (Stream Line Pro).

Deployment dates		Location				
Start	**End**	**Site-Facility**	**Latitude (deg North)**	**Longitude (deg East)**	**Altitude (m MSL)**	**Comment**
20160604	Present	OLI M1	70.494856	-149.88647	6	Top of trailer
20160503	20160524	SGP E37	36.310853	-97.9274278	389	Top of trailer

Table 11.   Deployment history for 0319-160 (Stream Line Pro).

Deployment dates		Location				
Start	**End**	**Site-Facility**	**Latitude (deg North)**	**Longitude (deg East)**	**Altitude (m MSL)**	**Comment**
20210609	Present	SGP E39	36.819656	-97.819869	6	Top of trailer
20190920	20201001	MOS M1	Ship-based deployment		~10	MOSAiC

Table 12.   Deployment history for 0720-193 (XR+).

Deployment dates		Location				
Start	**End**	**Site-Facility**	**Latitude (deg North)**	**Longitude (deg East)**	**Altitude (m MSL)**	**Comment**
20210715	Present	GUC-M1	38.956101	-106.987830	2889	SAIL
20200930	20210108	SGP S01	36.6052	-97.4857	314	Dual-mode @ C1
20200826	20200930	SGP E32	36.819656	-97.819869	335	Temporary replacement for 0514-83

Table 13.   Deployment history for 0921-214 (XR+).

Deployment dates		Location				
Start	**End**	**Site-Facility**	**Latitude (deg North)**	**Longitude (deg East)**	**Altitude (m MSL)**	**Comment**
20221109	Present	SGP S6	36.362322	-97.405108	329	AWAKEN site A1

Table 14.   Deployment history for 0921-215 (XR+).

Deployment dates		Location				
Start	**End**	**Site-Facility**	**Latitude (deg North)**	**Longitude (deg East)**	**Altitude (m MSL)**	**Comment**
20221007	Present	SGP S4	36.437039	-97.407744	307	AWAKEN site H
20220629	20220927	SGP E32	36.819656	-97.819869	335	Replacement for 83
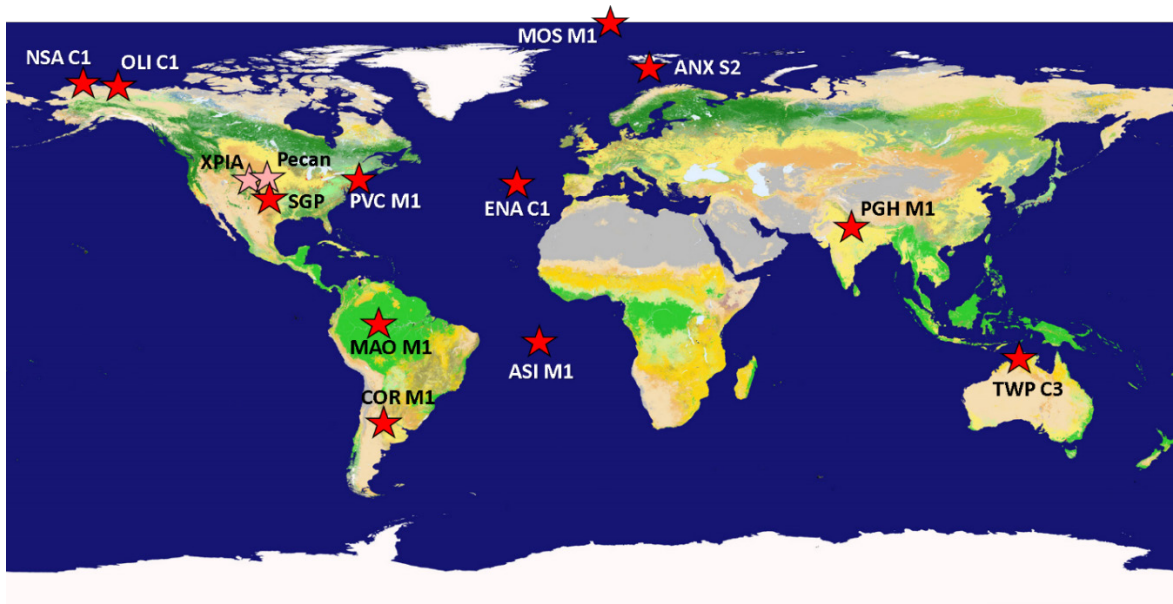
Table 15.   Deployment history for 0323-236 (XR+).

Deployment dates		Location				
Start	End	Site-Facility	Latitude (deg North)	Longitude (deg East)	Altitude (m MSL)	Comment
20221110	Present	n/a	36.361796	-97.381615	323	AWAKEN site A5

Table 16.   Deployment history for 0323-237 (XR+).

Deployment dates		Location				
Start	End	Site-Facility	Latitude (deg North)	Longitude (deg East)	Altitude (m MSL)	Comment
20221110	Present	n/a	36.347077	-97.389629	312	AWAKEN site A7

Figures 2 and 3 show the locations where ARM Doppler lidars have been or are currently deployed. These locations include the Southern Great Plains (SGP), North Slope of Alaska (NSA), Eastern North Atlantic (ENA), and Oliktok Point (OLI), as well as multiple deployments of the first and second mobile facilities (AMF1 and AMF2). Figure 3 shows the network of five Doppler lidar systems that existed at the SGP site from 2016 to 2022. In 2022 the profiling modules (and Doppler lidars) were removed from E32 and E41.

Figure 2.   Current and past deployment locations for the ARM Doppler lidars.

Figure 3. The network of five Doppler lidars at SGP includes one Halo Photonics Stream Line at each of the extended facilities (E32, E37, E39, and E41) and one XR and one XR+ at the Central Facility (C1).

4.0   Data Description

The ARM Doppler lidars can be configured to output processed and/or raw data. The processed data include range-resolved measurements of radial velocity, intensity (signal-to-noise ration [SNR]+1), and attenuated backscatter. The raw data include the Doppler spectra from which the processed data are obtained. Processed data are routinely logged, whereas raw data are only logged during selected IOPs due to the data volume.

Both processed and raw data are available (in netCDF format) for download using the ARM Data Discovery tool (https://adc.arm.gov/discovery/). This section describes the contents and format of the processed and raw data files.

4.1   Processed Data

Processed data files obey the following naming convention: <*site*>dl<*scan type*><*facility*>.b1, where <*site*> is the site name (e.g., sgp, nsa, ena, etc.), <*scan type*> is the scan type identifier, and <*facility*> is the facility designation (e.g., C1, E32, M1, S2, etc.)(ARM Standards Committee 2016). Seven scan type identifiers are currently in use: these are listed in Table 17.

Table 17.   Doppler lidar scan type identifier used in the datastream names.

Scan type identifier	Description
fpt	Fixed-beam stare. This can be either a slant-path or a vertical stare.
ppi	Single-pass full-360° plan position indicator scan
ppi2	Single- or multi-pass full or limited sector plan position indicator scan
rhi	Single-pass full-180° range height indicator scan
rhi2	Single- or multi-pass full or limited sector range height indicator scan
cal1	Calibration scan type 1
cal2	Calibration scan type 2

The format of all the processed data files is identical, regardless of the scan type. Table 18 lists the primary variables in these datastreams.

Table 18.   Primary variables in the \<site\>dl\<scan type\>\<facility\>.b1 datastream. These datastreams contain processed data that were generated in real time by the lidar's internal signal processor.

Variable	Dimensions	Units	Description
base_time	Scalar	s	Beginning of current day in seconds since 1970-1-1 0:00:00 0:00
time_offset	time	seconds	Time offset from base_time
range	range	m	Distance from lidar to the center of range gate
azimuth	time	deg	Beam azimuth angle measured clockwise from true north
elevation	time	deg	Beam elevation angle measured from horizonal
radial_velocity	time, range	$m\ s^{-1}$	Radial velocity, >0 for motion away from lidar
intensity	time, range	unitless	SNR+1
attenuated_backscatter	time, range	$m^{-1}\ sr^{-1}$	Attenuated backscatter

As is the convention with ARM, the time stamp for each beam (or profile) is given by the sum of the base time with the time offset. This gives the time of each profile in seconds since 00:00:00 UTC on 1 January, 1970. The variable 'range' is a one-dimensional array that specifies the distance from the lidar to the center of the range gates. The beam pointing direction is defined by the variables 'azimuth' and 'elevation'. The parameters called 'radial_velocity', 'intensity', and 'attenuated_backscatter' are 2-dimensional matrices (in time and range). Line-of-sight velocity measurements are stored in 'radial-velocity', and 'intensity', which is the SNR plus one, and provides a measure of the return signal strength. We should point out that the attenuated backscatter is derived from the SNR (intensity-1) using a factory-determined calibration curve, which we discuss in Section 6.4.1.

4.2 Raw Data

When raw data logging is enabled, the Halo Doppler lidar generates files containing specific elements of the return signal autocovariance matrix, from which the truncated autocovariance function (ACF) can be formed. The Doppler power spectrum is then obtained from the Fourier transform of the ACF. The advantage of storing the raw data in this way is that it allows for post-processing using any desired range gate size. Halo Doppler lidars can store the raw data in two different formats (Standard and AET [After Effects Project Template]). The main difference is that the AET format stores the hourly background data in each of the data files.

Raw data files obey the following naming convention: <site>dlacf<facility>.a0, where 'acf' is short for autocovariance function. When both processed and raw data are logged there is a one-to-one correspondence between processed and raw data file names. The only difference, aside from the extension, is that the raw file names do not include a scan type identifier. Thus, the date and time strings are the only way to establish correspondence between raw and processed files. Table 19 provides an example using data collected between 15 and 16 UTC on 14 December 2018, during ARM's Cloud, Aerosol, and Complex Terrain Interactions (CACTI) campaign in Argentina. This table lists the processed files that were collected and the corresponding raw file names. We note that the start times can differ by about 1 s or so between the raw and processed file names.

Table 19. Processed and raw files collected between 15 and 16 UTC during CACTI on 14 December 2018.

Processed file name	Corresponding raw file name
cordlppiM1.b1.20181214.150015.cdf	cordlacfM1.a1.20181214.150014.nc
cordlfptM1.b1.20181214.150055.cdf	cordlacfM1.a1.20181214.150055.nc
cordlppiM1.b1.20181214.151505.cdf	cordlacfM1.a1.20181214.151504.nc
cordlppiM1.b1.20181214.153005.cdf	cordlacfM1.a1.20181214.153004.nc
cordlppiM1.b1.20181214.154505.cdf	cordlacfM1.a1.20181214.154504.nc

The primary variables in the <site>dlacf<facility>.a0 datastream are listed below in Table 20. Ungated autocovariances for each beam are stored in the variable called 'acf', and the autocovariances of the background noise are stored in the variable called 'acf_bkg'. Note that the system automatically acquires a background measurement when it starts up, and at the top of each hour of operation. The most recent background data are included in all the raw data files.

Table 20. Primary variables in the <site>dlacf<facility>.a0 datastream.

Variable	Dimensions	Units	Description
base_time	Scalar	s	Beginning of current day in seconds since 1970-1-1 0:00:00 0:00
time_offset	time	s	Time offset from base_time
azimuth	time	deg	Beam azimuth angle measured clockwise from true north
elevation	time	deg	Beam elevation angle measured from horizonal

Variable	Dimensions	Units	Description
acf_bkg	nsamples, nlags, complex	unitless	Ungated ACF of the noise background
acf	time, nsamples, nlags, complex	unitless	Ungated ACF
wavelength	Scalar	nm	1548
sampling_rate	Scalar	MHz	50

From Table 20 we see that 'acf' is a 4-dimensional quantity, where the last dimension specifies real and imaginary parts. So we can think of 'acf' as a 3-dimensional complex quantity, where the three dimensions specify time, range, and lag, respectively. The number of samples in the range dimension is 'nsamples', and the number of lags used to approximate the ACF is 'nlags'. Specific values for 'nsamples' and 'nlags' are system dependent, as indicated in Table 16. For the Stream Line, XR, and XR+ models, the value of 'nsamples' is independent of how the lidar operator configures the system. For the Pro systems, nsamples is determined by the product of the number of gates with the number of samples per gate, which are set by the lidar operator. We also note that the Pro systems do not include background data in the raw output files.

The raw files also include the wavelength and the sampling rate used to acquire the raw in-phase and quadrature (I&Q) signal data. From this one can compute the range vector and the Nyquist velocity. The spacing between I&Q samples is given by

$$\Delta r = \frac{c}{2 f_s} \tag{1}$$

where c is the speed of light and f_s is the sampling rate. All the ARM Doppler lidars sample the return signal at 50 MHz. For f_s = 50 MHz the spacing between samples is 3 m. The range vector can then be computed as $r_j = j \Delta r$, for $j = 0 \ldots$ nsamples-1. Also, the Nyquist velocity is given by

$$u_{Nyquist} = \lambda f_s / 4, \tag{2}$$

which is equal to 19.4 ms^{-1} for λ = 1548 nm and f_s = 50 MHz. We note that the passband width is $\lambda f_s / 2$, where $f_s / 2$ is the Nyquist frequency. However, after shifting to baseband (see Section 6.1) the radial velocity measurement range becomes $\pm \lambda f_s / 4$.

Table 21. The number of samples in the range dimension (nsamples) and the number lags (nlags) used to represent the ungated ACFs in the raw data files (AET format). For the Pro systems, nsamples is determined by the product of the number of gates, M, with the number of samples per gate, N, which are set by the lidar operator. Also shown are the pulse repetition frequencies and the corresponding maximum unambiguous ranges for all of the ARM Doppler lidars.

Serial number	Model	nlags	nsamples	Background included?	PRF (kHz)	Maximum unambiguous range (km)
0910-07	Stream Line	7	3200	Yes	15	10
0910-08	Stream Line	7	3200	Yes	15	10
0910-09	Stream Line	7	3200	Yes	15	10
0514-82	Stream Line Pro	7	N x M	No	15	10
0514-83	Stream Line	7	3200	Yes	15	10
0514-84	Stream Line	7	3200	Yes	15	10
0116-107	XR	20	4000	Yes	15	15
0116-108	Stream Line	7	4000	Yes	15	10
0116-109	Stream Line Pro	7	N x M	No	15	10
0319-160	Stream Line Pro	7	N x M	No	15	10
0720-193	XR+	20	4000	Yes	10	15
0921-214	XR+	20	4000	Yes	10	15
0921-215	XR+	20	4000	Yes	10	15
0322-236	XR+	20	4000	Yes	10	15
0322-237	XR+	20	4000	Yes	10	15

4.2.1   Autocovariance Data

The lidar's real-time signal processor computes the various elements of the autocovariance matrix of the I&Q signal for each laser pulse. It then averages these elements over some prescribed number of laser pulses and stores the results. The Doppler power spectrum is obtained from the Fourier transform of the ACF. The ACF is formed by summing the appropriate elements of the autocovariance matrix. In this subsection we explain how to use this raw ACF data to generate the Doppler power spectrum.

After the pulse leaves the lidar, the return signal is mixed with the local oscillator (LO), subjected to complex demodulation, and then sampled at 50 MHz (see Section 6.1). This produces a complex signal where the real and imaginary parts are referred to as the in-phase (I) and quadrature components (Q), respectively. We represent the complex digitized signal as

$$f_j = I_j + iQ_j \tag{3}$$

Where $i = \sqrt{-1}$ and j is a range index that runs from 0 to nsamples-1 (see Table 16). The kth lag of the ungated ACF is given by

$$\gamma_k = \frac{1}{N-k} \sum_{j=0}^{N-k-1} \overline{f_j f_{k+j}^*} \tag{4}$$

where N is the number of samples in the range dimension, i.e., 'nsamples' in Table 16. The overbar in equation (4) indicates averaging over the pulse integration period. To simplify the notation we let

$$s_{jk} = \frac{\overline{f_j f_{k+j}^*}}{N-k}. \tag{5}$$

Range-resolved measurements of velocity and SNR are obtained from the gated ACF. The kth lag of the gated ACF is obtained by summing over the appropriate range samples of the ungated ACF, i.e.,

$$\gamma_{km} = \sum_{j=m-n/2}^{m+n/2} s_{jk}. \tag{6}$$

where n is the number of samples in each range gate, and m is a range sample index that defines the center of the range gate. As an example, let us say we are interested in obtaining the ACF at a range of 1000 m from the lidar using a 30-m range gate. As stated previously, the spacing between I&Q samples is 3 m for all of the ARM DLs. Thus, there are $n=10$ range samples in a 30-m range gate, and the center of the range gate would be given by $m=333$.

At this point we need to distinguish between atmospheric measurements and noise or background measurements. The ARM DLs automatically acquire background data at the top of every hour of operation. For the Stream Line and Stream Line XR systems, this background measurement is made by staring downward at the top of the lidar enclosure, thereby effectively blocking the beam. For the Stream Line Pro this is accomplished by directing the beam away from the exit window. This noise measurement is then used to correct for systematic variations in the noise floor of the Doppler spectrum over the next hour, until a new background is acquired. The gated background (bkg) and atmospheric (atm) ACFs are denoted by

$$\gamma_{km}^{bkg} = \sum_{j=m-n/2}^{m+n/2} s_{jk}^{bkg} \tag{7}$$

and

$$\gamma_{km}^{atm} = \sum_{j=m-n/2}^{m+n/2} s_{jk}^{atm}, \tag{8}$$

respectively. The raw (uncorrected) atmospheric power spectrum for a range gate centered on the mth sample is obtained from the discrete Fourier transform of γ_{km}^{atm}, i.e.,

$$P_{lm}^{atm} = \sum_{k=0}^{N_{fft}-1} \gamma_{km}^{atm} e^{i2\pi kl/N_{fft}} \quad , \tag{9}$$

where N_{fft} is the number of points in the discrete Fourier transform. Likewise, the noise spectrum is obtained from

$$P_{lm}^{bkg} = \sum_{k=0}^{N_{fft}-1} \gamma_{km}^{bkg} e^{i2\pi kl/N_{fft}} \tag{10}$$
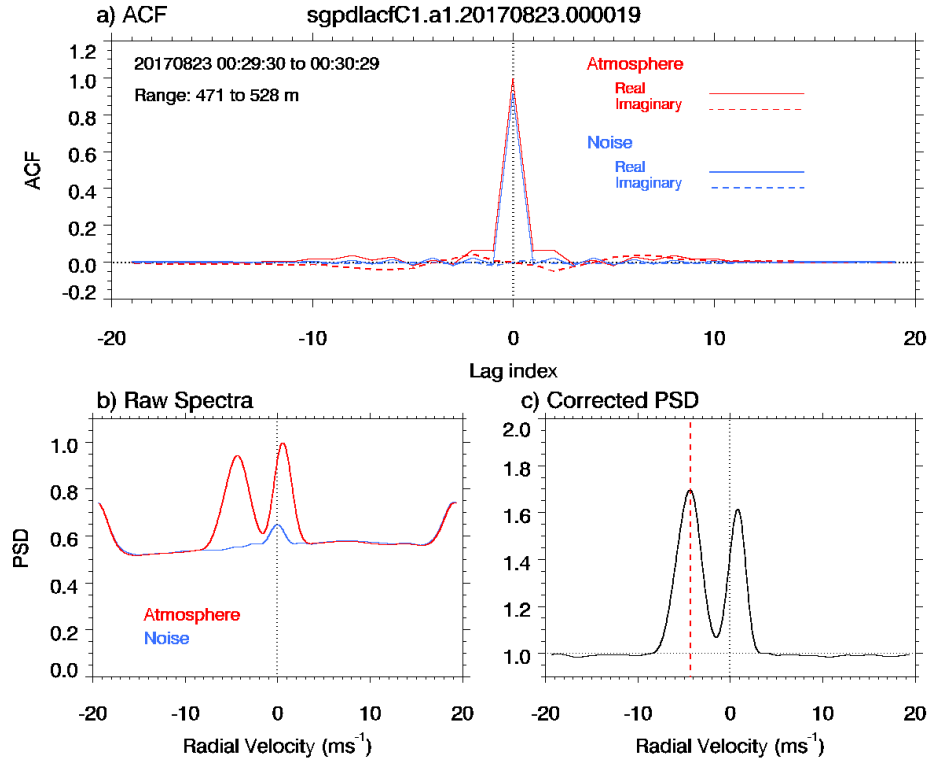
The final (noise floor) corrected Doppler spectrum is then obtained from

$$P_{lm} = \frac{P_{lm}^{atm}}{P_{lm}^{bkg}} \quad . \tag{11}$$
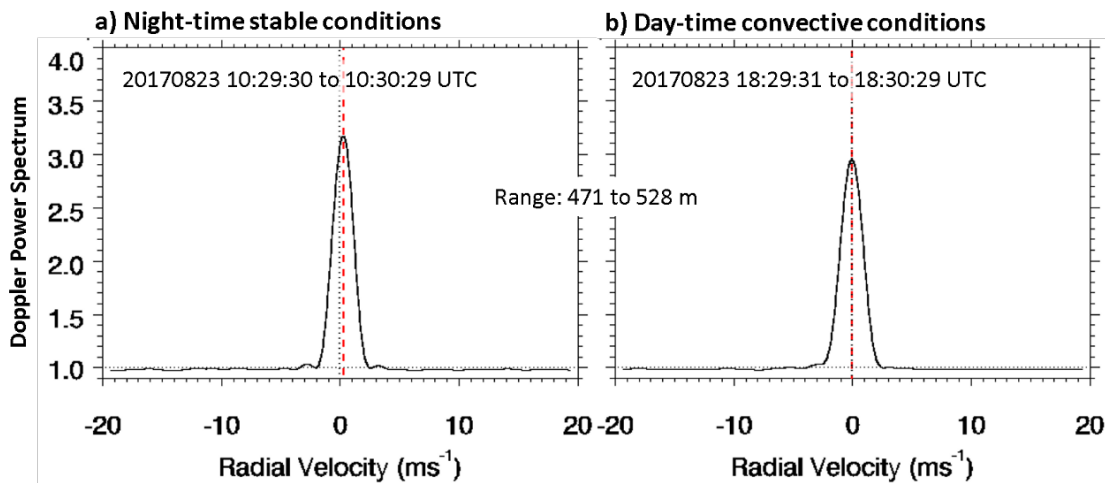
In practice, the ACFs are zero padded out to N_{fft}, and then transformed using a fast Fourier transform (FFT) algorithm. The number of FFT points is configurable, but typically we use N_{fft}=1024, as recommended by Halo Photonics. Since the ACFs are only defined out to *nlags* (which is either 7 or 20 depending on the system), there is a considerable amount of zero padding, which result in smooth spectra.

Figure 4a shows examples of gated ACFs for the background and atmospheric measurements. The raw atmospheric and background spectra are shown in Figure 4b, and the final noise-floor-corrected Doppler spectrum is shown in Figure 4c. This example was taken from data collected by the Doppler lidar at SGP C1 on 23 August 2017 at about 00:30:00 UTC, while staring vertically during a precipitation event. The corrected Doppler spectrum shows two distinct modes, one associated with the falling rain drops, and one associated with the air motion. The dashed red line indicates the radial velocity associated with the global maximum, which in this case is the apparent fall speed of precipitation.

Figure 5 shows corrected Doppler spectra acquired under stable and unstable conditions. Both of these spectra were computed using an averaging time of 60 s and a 60-m range gate centered at 500 m AGL. Qualitatively, we can see there is not a lot of difference between the two spectra in Figure 5, indicating that the spectral shape (e.g., spectral width) is not significantly affected by atmospheric stability.

Figure 4.   Examples of a) the autocovariance function, b) the raw atmospheric and noise spectra, and c) the noise-floor-adjusted atmospheric Doppler spectrum. This example was taken from data collected by the Doppler lidar at SGP C1 on 23 August 2017 at about 00:30:00 UTC. Precipitation was occurring in this time period. The corrected Doppler spectrum shows two distinct modes, one associated with the falling rain drops, and one associated with the air motion. The dashed red line indicates radial velocity associated with the global maximum, which in this case is the apparent fall speed of the precipitation.

Figure 5.   Examples of Doppler spectra acquired under a) stable nocturnal conditions, and b) daytime convective conditions. Both of these spectra were obtained at 500 m AGL using a 60-m range bin and a 60-s averaging time.

For the Halo lidars, the Doppler shift is obtained by simply finding the frequency corresponding to the global maximum in the Doppler power spectrum. Since no attempt is made to interpolate between frequencies, the resolution of the velocity estimate is determined by the number of points in the FFT, together with the wavelength and the sampling rate. For $\lambda = 1548$ nm, $f_s = 50$ MHz, and $N_{FFT} = 1024$ the velocity measurement resolution is $\lambda f_s / (2 N_{fft}) = 0.038$ ms^{-1}, i.e., the receiver bandwidth divided by N_{FFT}.

Another important point is that there is, in general, a small systematic bias or offset in the Doppler velocities derived from the Doppler spectra. These offsets, which are fixed for a given system, are determined at the factory. Table 17 lists the velocity offsets for each of the ARM systems. When estimating radial velocities from the Doppler spectra one should add this offset to the result, i.e.,

$$u_r = u_r' + u_{offset} \tag{12}$$

where u_r' is the velocity corresponding to the global maximum in the Doppler spectrum, u_{offset} is the radial velocity offset parameter listed in Table 17, and u_r is the final "unbiased" radial velocity estimate.

Table 22.   Radial velocity offset parameter for each of the ARM Doppler lidars.

Serial number	u_{offset} (ms^{-1})
0910-07	0.45
0910-08	0.45
0910-09	0.0
0514-82	0.25
0514-83	0.34
0514-84	0.0
0116-107	0.0
0116-108	0.058
0116-109	0.5
0319-160 through 0322-237	0.0

For a given beam, the variable called 'acf' in the raw data files (see Table 15) is the same as s_{jk}^{atm}. That is, for a given time index, i, we have

$$\text{acf}[i,j,k,0] = real(s_{jk}^{atm})$$

$$\text{acf}[i,j,k,1] = imaginary(s_{jk}^{atm}).$$

Likewise, the variable called 'acf_bkg' in the raw data files (see Table 15) is the same as s_{jk}^{bkg} , i.e.,

$$\text{acf\_bkg}[j,k,0] = real(s_{jk}^{bkg})$$

$$\text{acf\_bkg } [j,k,1] = imaginary(s_{jk}^{bkg}) .$$

4.2.2   Background Data

The ARM Doppler lidars also generate so-called background data. The datastream name for these files is
<site>dlbackground<facility>.a0. These data files store the hourly profiles of the noise or background
signal strength for a given day. Noise measurements are made at the top of each hour of operation, so the
background files typically contain 24 profiles. Specifically, these files contain the (real) zeroth lag of the
gated ACF for the background noise measurement, i.e.,

$$\gamma_{0m}^{bkg} = \sum_{j=m-n/2}^{m+n/2} s_{j0}^{bkg} . \tag{13}$$

Although these data are not widely used, Manninen et al. 2016 has shown their utility for correcting the
processed SNR for systematic variations in the background noise. Table 23 lists the primary variables in
the background datastream.

Table 23.   Primary variables in the <site>dlbackground<facility>.a0 datastream.
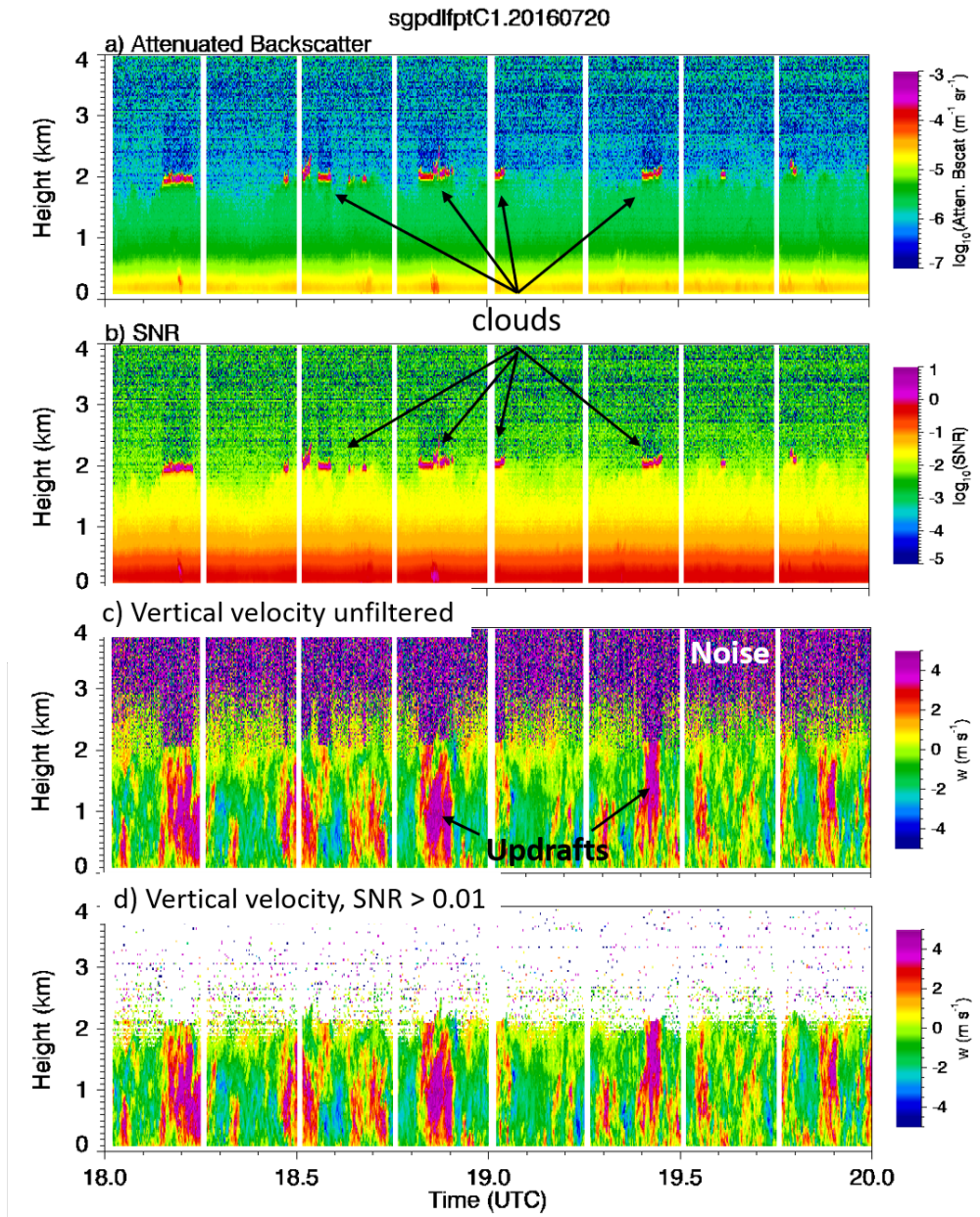
Variable	Dimensions	Units	Description
base_time	Scalar	s	Beginning of current day in seconds since 1970-1-1 0:00:00 0:00
time_offset	time	s	Time offset from base_time
gate	range	unitless	Range index 0...400
background	time, range	unitless	Zeroth lag of the gated ACF for the background

4.3   Value-Added Products
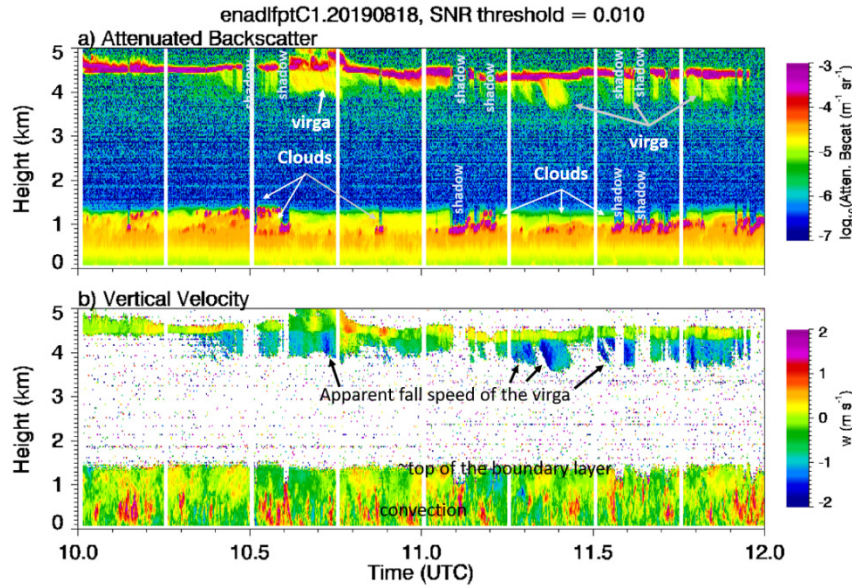
Two value-added products (VAPs) are currently being generated operationally that use ARM Doppler
lidar data. These include the wind VAP (Newsom et al. 2017, Newsom et al. 2019a), and the vertical
velocity statistics VAP (Berg et al. 2017, Newsom et al. 2019b). The wind VAP uses the PPI scan data to
compute profiles of wind speed and direction. The vertical velocity statistics VAP uses the vertical staring
data to derive 30-min averages of vertical velocity variance, skewness, and kurtosis, as well as cloud-base
height, cloud-base vertical velocity, and cloud fraction.

4.4   Annotated Examples
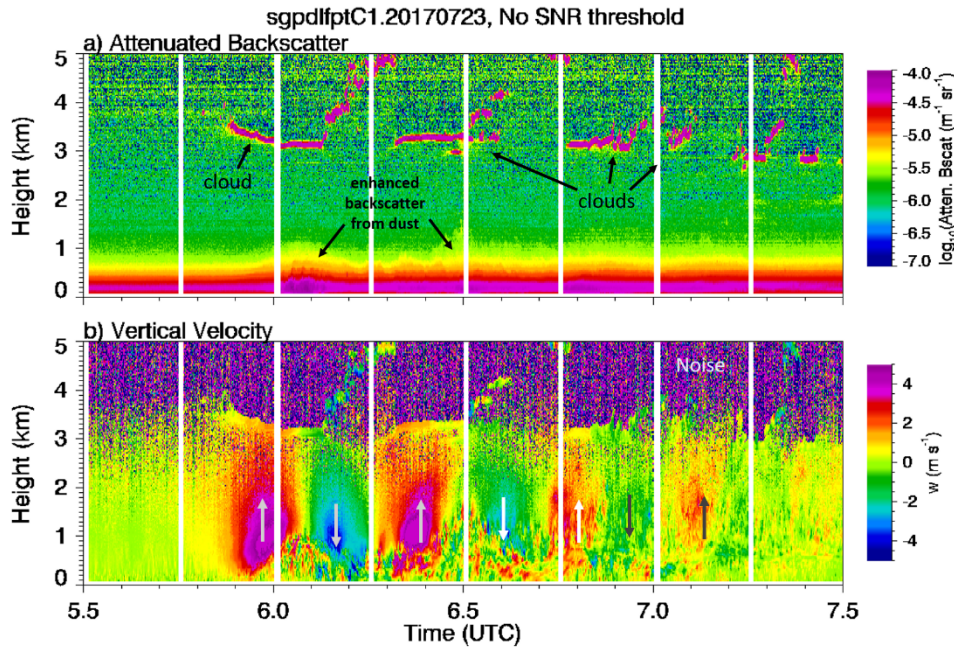
Figures 6 through 11 show annotated examples of processed data from vertical stares performed by the ARM Doppler lidars. In many of these examples, a minimum SNR threshold of either 0.01 or 0.008 was used to filter the velocities. Depending on the application, data users may also need to apply an upper threshold to filter out instances such as dense fog, cloud, or hard-target returns when scanning.
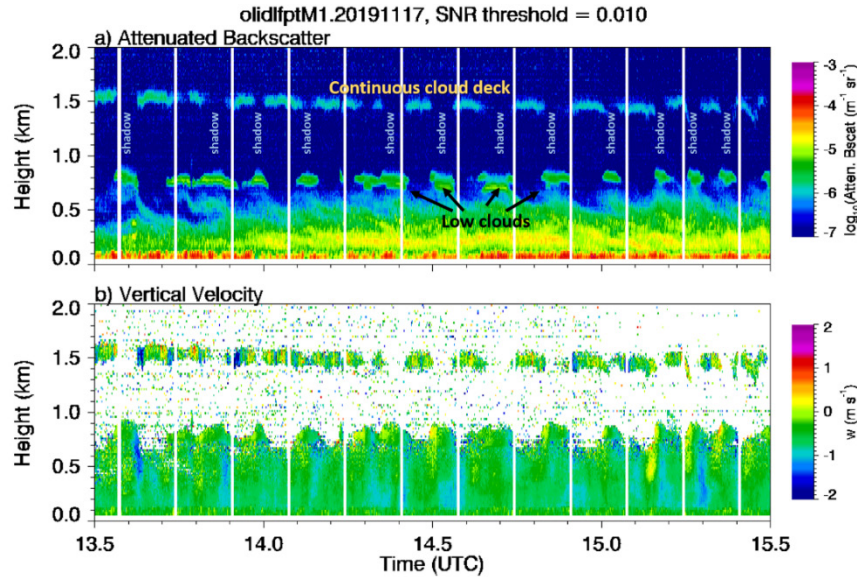
Figure 6.   Examples of a) attenuated backscatter, b) SNR, c) unfiltered vertical velocity, and d) vertical velocity for SNR > 0.01. These examples were taken from the 0116-107 system at SGP C1 on 20 July 2016, when the convective boundary layer was at its maximum depth for this day. Panel d) illustrates how SNR thresholding can be used to eliminate much of the poor-quality velocity data. The white vertical bands in each panel are time periods when other (PPI) scans were being performed.
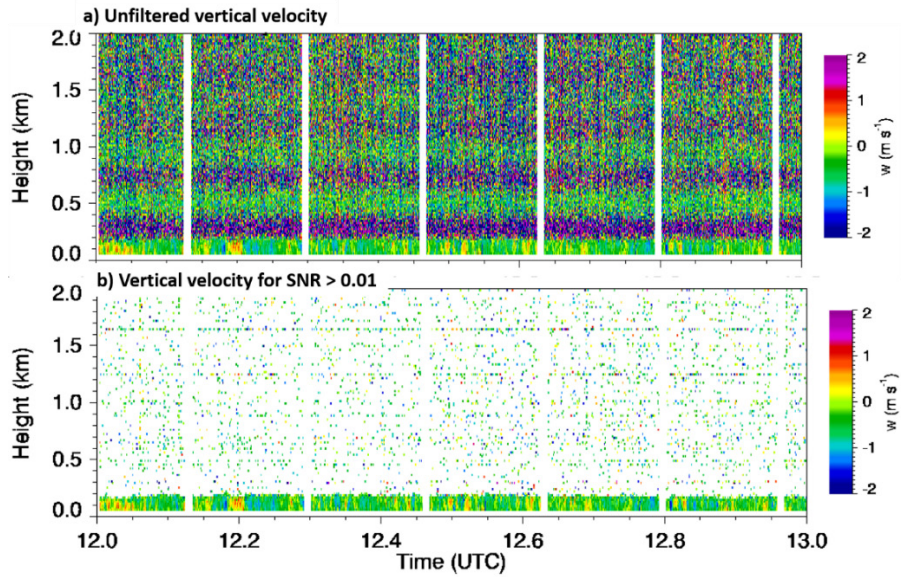
Figure 7. a) Attenuated backscatter, and b) vertical velocity observed by the 0514-84 system at ENA C1 between 10 and 12 UTC on 18 August 2019. This example shows shallow cumulus forming near the top of the boundary layer and underneath a higher-level cloud deck at about 4.5 km AGL. Precipitation (virga) is seen falling from the higher-level cloud deck. The white vertical bands are time periods when other (PPI) scans were being performed. An SNR threshold of 0.01 was used to filter the velocities in panel.
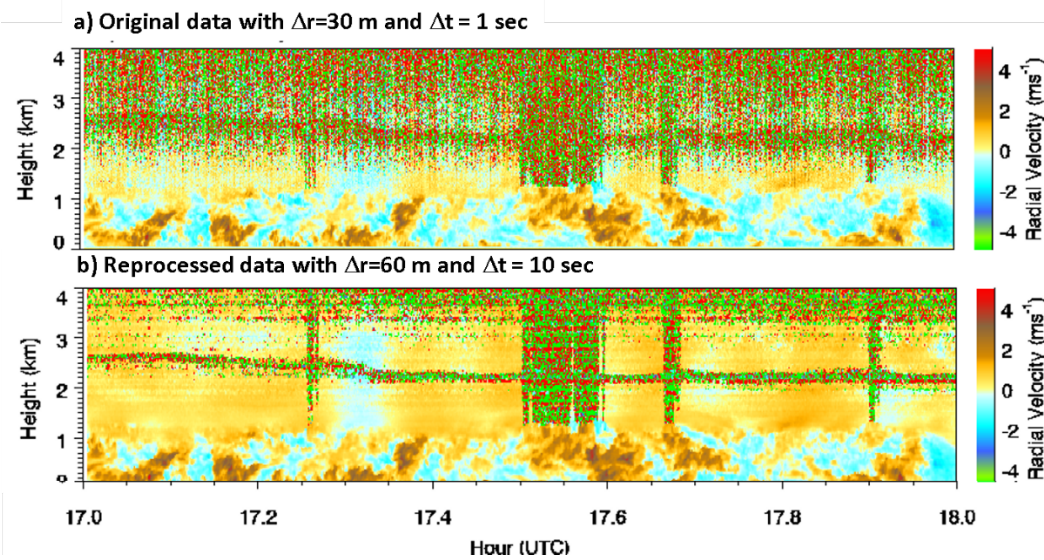
Figure 8. a) Attenuated backscatter, and b) vertical velocity as observed by the 0116-107 system at SGP C1 between 05:30 and 07:30 UTC on 23 July 2017. In this case a rather intense gravity wave is seen propagating over the site. The white vertical bands are time periods when other (PPI) scans were being performed.

Figure 9. a) Attenuated backscatter, and b) vertical velocity as observed by the 0116-109 system at Oliktok Point, Alaska between 13:30 and 15:30 UTC on 17 November 2019. This example shows what appears to be some sort of gravity wave or shear-flow instability propagating over the site. The white vertical bands are time periods when other (PPI) scans were being performed.

Figure 10. a) Unfiltered vertical velocity, and b) vertical velocity for SNR > 0.01 as observed by the 0116-109 system at Oliktok Point, Alaska between 12 and 13 UTC on 3 October 2019. Panel a) shows what appears to be some sort of artifact in the vertical velocity that varies sinusoidally with height. Filtering the vertical velocity based on the SNR effectively removes the velocity affected by these artifacts. For panel b), an SNR threshold of 0.01 was used. In this example, valid measurements are mostly confined below 200 m.

Figure 11. This example shows how the range performance can be improved through reprocessing raw data. Panel a) shows the original 1-sec and 30-m (processed) vertical velocities from the 0116-107 system at SGP C1 on 27 August 2017. Panel b) shows the result of reprocessing the raw data with a range gate size of 60 m, and temporal resolution of 10 sec.

4.5 Quiklook Plots

Data collected by the ARM DLs can be viewed by accessing the web site maintained by the ARM Data Quality Office (https://dq.arm.gov/dq-plotbrowser/). This site provides an interactive web-based tool for plotting radial velocity, attenuated backscatter, and intensity (SNR+1) from the Doppler lidars. Additionally, the instrument mentors maintain a site (https://engineering.arm.gov/~newsom/Doppler) where plots of vertical velocity, SNR, winds, and vertical velocity statistics can be viewed.

5.0 Data Quality and Availability

This section discusses data availability, measurement uncertainty, and data quality. This includes an assessment of the velocity bias for both hard and diffuse targets, velocity precision, and beam pointing accuracy.

5.1 Data Availability

Table 24 shows the data availability for vertical staring data from all of the ARM DLs. The data availability represents the percentage of valid samples (exceeding SNR > 0.008) below a given altitude, as indicated in Table 24. These numbers were obtained by averaging over specific time periods that differ from system to system. The time periods and the deployment locations are also given in the table. We note that the XR at SGP C1 (S/N 0116-107) has the highest data availability, and the two arctic systems (S/N 0116-108 and 0514-82) have the lowest data availability, as expected.

Table 24. Data availability for several ARM Doppler lidar systems. The data availability is the percentage of measurements with SNR>0.008 below a given height (AGL).

Serial number	Data availability (%)				Location	Year
	<500 m	**< 1000 m**	**< 2000 m**	**< 3000 m**		
0910-07	96.61%	88.43%	55.28%	38.44%	SGP E41	2017
0910-08	98.50%	92.57%	63.80%	45.18%	SGP E39	2017
0910-09	93.40%	70.85%	40.08%	27.91%	ASI M1	2016/17
0514-82	71.17%	51.55%	35.85%	28.80%	NSA C1	2017
0514-83	96.75%	89.22%	57.42%	39.81%	SGP E37	2017
0514-84	98.73%	93.42%	64.77%	44.92%	ENA C1	2019
0116-107	98.86%	92.40%	64.67%	45.77%	SGP C1	2017
0116-108	91.08%	83.84%	57.63%	40.57%	SGP E32	2017
0116-109	74.17%	53.21%	34.85%	26.82%	OLI M1	2017

5.2 Anemometer Comparison
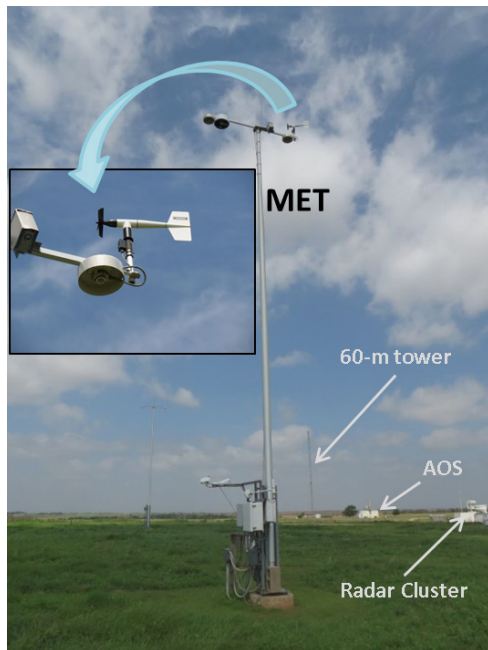
In June 2014 two newly acquired systems (0514-83 and 0514-84) were tested at SGP C1. As part of that testing, the measurements from the lidars were compared to measurements from a Young wind sensor mounted on top of the 10-m surface meteorological tower (i.e., sgpmetE13.b1). For this test, the two lidars were deployed at two different locations within the Central Facility and both lidars directed their beams to a common point near the anemometer, as shown in Figure 12. The data from the two lidars were then processed to produce estimates of wind speed and direction, which were then compared to the Young wind sensor measurements.

Figure 12 shows the locations of the 0514-83 and 0514-84 lidars and the 10-m meteorological tower. As indicated, the surface meteorological tower is located near the south-eastern corner of Figure 12, the 0514-83 lidar was deployed 402 m to the north-northwest, near the main access road, and the 0514-84 lidar was deployed 288 m to the west-northwest of the met tower, near the north side of the Aerosol Observing System. The angle between the two lidar beams was about 38°.
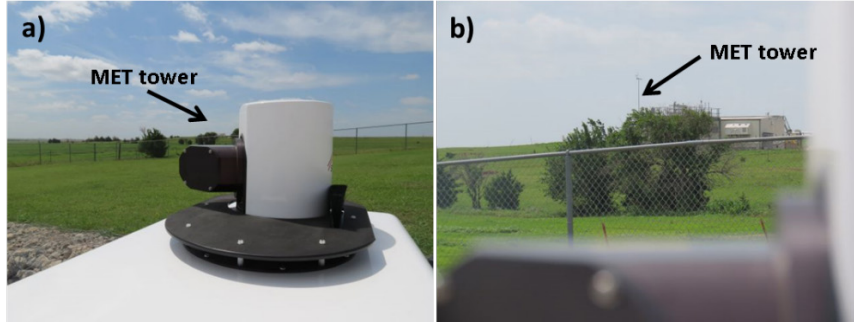
Figure 12. Instrument placement during the lidar-anemometer comparison test at SGP C1 in June 2014.
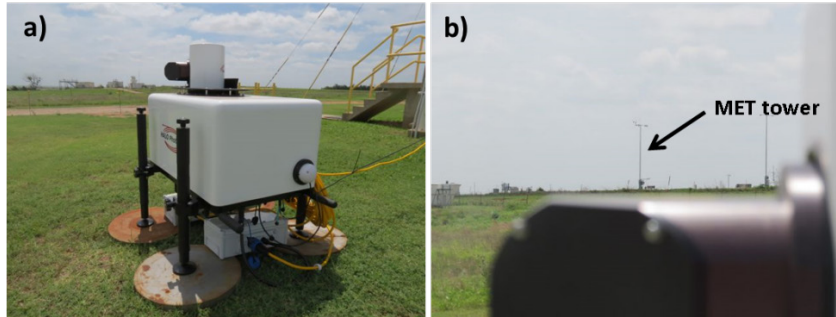
Pointing accuracy was obviously important for this test. Each lidar was leveled to within 0.1°, and the headings with respect to true north were determined using the method described in Section 6.4.2.1.

Figure 13. The 10-m meteorological tower at SGP C1. The inset shows the Young wind sensor at the 10-m level.
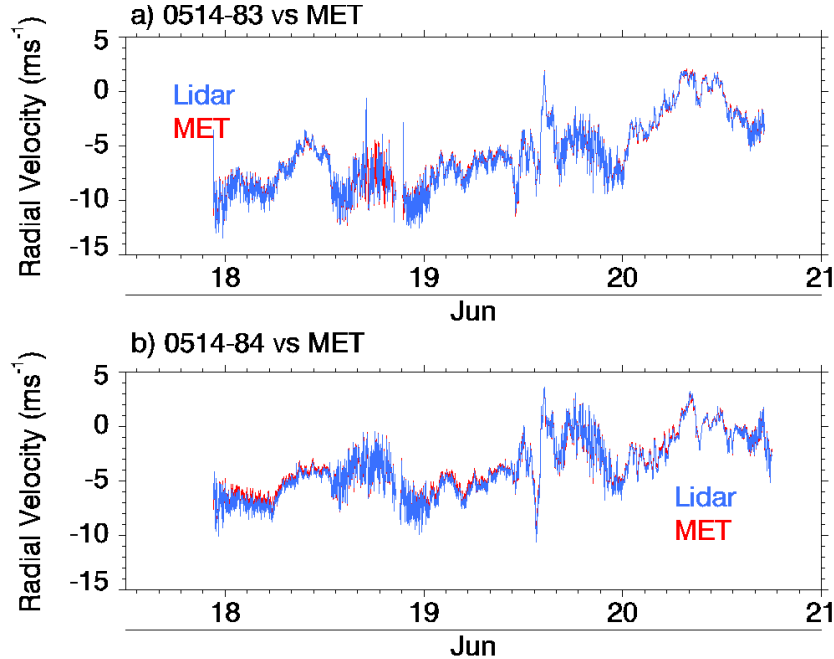
Figure 14. Looking toward the 10-m meteorological tower from the 0514-83 Doppler lidar at SGP C1.
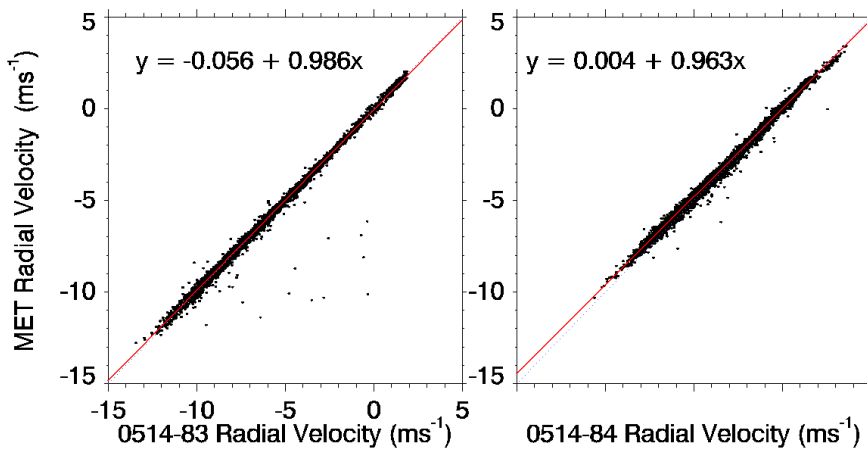
Figure 15. Looking toward the 10-m meteorological tower from the 0514-84 Doppler lidar at SGP C1.

The dual-Doppler-anemometer-stare test was run from about 2230 UTC on 17 June to about 1830 UTC on 20 June 2014. During this period both lidars were operated using 15000 pulse averages (i.e., 1 sec), 30-m range gates, and a focus range of 1000 m. Meteorological conditions during this three-day test were typical for the locale and time of year. A strong southerly flow dominated the daytime period (with winds commonly in excess of 10 ms^{-1}), with lighter winds at night. Light rain occurred on the morning of 19 June.

First, we compared the radial velocities from each lidar to the corresponding line-of-sight velocity components from the 1-min tower data (i.e., the sgpmetE13.b1 datastream). This required interpolating the radial velocities along the beams to the intersection point. These velocities were then averaged in time to match the sample times and temporal resolution of the anemometer data (i.e., 1-min resolution). Figure 16 displays a comparison between the time series from the lidars and the met tower anemometer, and Figure 17 shows the corresponding correlation diagrams.

Figure 16. 1-min average radial velocities from the lidars (blue) compared to the corresponding 1-min average radial component of the anemometer winds (red) for a) 0514-83 versus anemometer, and b) 0514-84 versus anemometer.

Figure 17. Correlation diagram showing comparison between a) the average line-of-sight component of the anemometer versus the radial velocity measurements from 0514-83, and b) the line-of-sight component of the anemometer versus the radial velocity measurements from 0514-84.

For the 0514-83 system the radial velocity measurement bias was -2 cm s^{-1}, the standard deviation of the difference was 38 cm s^{-1}, and the Pearson coefficient of linear correlation was 0.993. Here the bias is defined such that a positive value implies that the lidar velocities are greater than the anemometer velocities. For 0514-84 the radial velocity measurement bias was -3 cm s^{-1}, the standard deviation of the difference was 24 cm s^{-1}, and the Pearson coefficient of linear correlation was 0.997.

The radial velocity measurements from the each of the lidars were combined in a dual-Doppler analysis to produce estimates of wind speed and direction at the intersection of the two beams. In the following, we use the subscript "83" to refer to the 0514-83 system, and the subscript "84" to refer to the 0514-84 lidar. Neglecting the vertical velocity, the radial velocity measured by each lidar can be expressed as

$$u_{r83} = \cos\theta_{83} \sin\phi_{83} u + \cos\theta_{83} \cos\phi_{83} v \tag{14}$$

and

$$u_{r84} = \cos\theta_{84} \sin\phi_{84} u + \cos\theta_{84} \cos\phi_{84} v \tag{15}$$

where u is the (unknown) eastward wind velocity component, v is the (unknown) northward wind velocity component, θ_{83} (θ_{84}) is the beam elevation angle for the 0514-83 (0514-84) lidar, and ϕ_{83} (ϕ_{84}) is the beam azimuth angle for the 0514-83 (0514-84). Equations (14) and (15) can be inverted to yield solutions for u and v. The result is

$$u = \left(\hat{u}_{r83} \cos\phi_{84} - \hat{u}_{r84} \cos\phi_{83} \right) / \Delta \tag{16}$$

and

$$v = \left(\hat{u}_{r84} \sin\phi_{83} - \hat{u}_{r83} \sin\phi_{84} \right) / \Delta \tag{17}$$

where
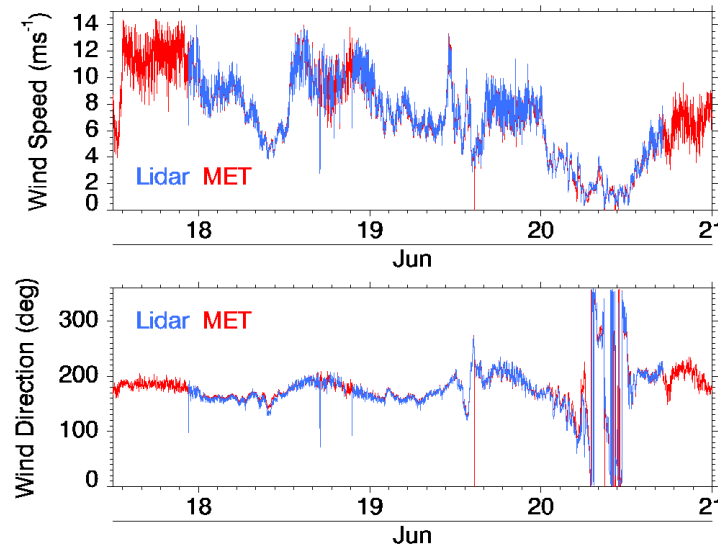
$$\Delta = \sin\phi_{83} \cos\phi_{84} - \cos\phi_{83} \sin\phi_{84} \tag{18}$$

$$\hat{u}_{r83} = u_{r83} / \cos\theta_{83} \tag{19}$$
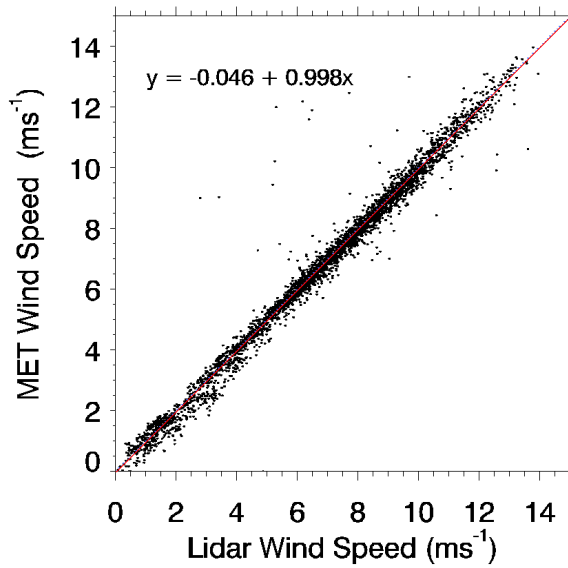
and

$$\hat{u}_{r84} = u_{r84} / \cos\theta_{84} . \tag{20}$$

Figure 18 shows a comparison between lidar-derived wind speed and direction using equations (16) and (17), and the wind speed and direction data from the anemometer. Also, Figure 19 shows a correlation diagram of the lidar-derived wind speed versus the anemometer wind speed. Linear regression yields an offset of -4.6 cm s^{-1}, and a slope of 0.998, indicating very good agreement between the dual-Doppler winds and the anemometer measurements. The results of the dual-Doppler lidar test are also summarized in Table 25.

Figure 18. Comparison dual-Doppler winds (blue) and anemometer measurements for a test conducted at SGP C1 from 17 to 21 June 2014.

Figure 19. Correlation diagram showing a comparison between the dual-Doppler-derived wind speed and the wind speed measured by the Young wind sensor on the top of the 10-m meteorological tower at SGP.

Table 25. Results of the dual-Doppler-anemometer comparison.

Wind speed bias (lidar-anemometer)	5.8 cm s^{-1}
Wind speed difference standard deviation	41.3 cm s^{-1}
Wind direction bias (lidar-anemometer)	-4.7º
Wind speed lidar correlation	0.990
Wind direction difference standard	44.5º

5.3 Bias from Hard Targets

When the lidar's beam is directed towards a stationary hard target (such as a building, tower, etc.), the radial velocity measurement at that location should be equal to 0 m/s. In this section we evaluate the velocity measurement bias using data that are routinely collected by the lidars. Specifically, we use hard-target scan data that is acquired on a once-per-day basis, as described in Section 6.4.2.1. Although these scans are used to help determine and monitor the heading of the lidar, they are also useful for evaluating the hard-target bias. Figure 29 in Section 6.4.2.1 shows an example of one such hard-target scan.

Here we analyze the daily hard-target scans from five Doppler lidars deployed at the SGP site (at C1, E32, E37, E39, and E41) for the period from 2012 through 2019. For a given scan, a gradient SNR filter is used to identify the hard target. If multiple hard targets are observed within the zone of interest, the radial velocity estimate closest to zero is selected for the bias estimate. These daily bias estimates were then used to compute the mean bias and standard deviation over the entire analysis period.

Table 26. Absolute mean radial velocity bias, μ_{rv}, and standard deviation, σ_{rv}, for measurements against hard targets at SGP.

SGP site	μ_{rv} (cm s^{-1})	σ_{rv} (cm s^{-1})	Period of observation
C1	0.48	8.20	October 2010–November 2019
E32	1.78	1.54	May 2016–November 2019
E37	-5.96	33.86	May 2016–November 2019
E39	-0. 76	4.09	May 2016–November 2019
E41	-7.14	7.49	May 2016–November 2019

5.4 Radial Velocity Precision

The random error in the observed radial velocities can be estimated from an analysis of radial velocity time series obtained from staring data (i.e., scan type = 'fpt'). To accomplish this, we make use of the technique described by Lenschow et al. (2000) and Pearson et al. (2009). To apply this method, we analyze velocity data at a fixed range over a given period of time (e.g., 30 min is typical).

The observed radial velocity from the ARM Doppler lidars can be expressed as

$$\hat{u}_r = u_r + n \qquad (21)$$

where u_r is the true atmospheric radial velocity, and n is the noise. We assume that the noise is a zero-mean Gaussian random and variable. If the noise is uncorrelated with u_r then the observed variance is given by

$$\sigma_{\hat{u}_r}^2 = \sigma_{u_r}^2 + \sigma_n^2 \qquad (22)$$

where $\sigma_{u_r}^2$ is the true atmospheric variance, and σ_n^2 is the variance of the noise. The noise generally increases with increasing range and decreasing SNR.

The autocovariance of the observed time series is given by

$$\hat{F}_i = \frac{1}{N-i} \sum_{j=0}^{N-1-i} \hat{u}'_{rj} \hat{u}'_{ri+j} , \qquad (23)$$

where i is the lag index, N is the number of samples in the time series, and $\hat{u}'_{rj}$ is the observed perturbation radial velocity, i.e., $\hat{u}'_{rj} = \hat{u}_{rj} - \overline{u_r}$. The variance of the observed velocities is then given by the zeroth lag of equation (23), i.e., $\sigma_{\hat{u}_r}^2 = \hat{F}_0$. Likewise, the ith lag of autocovariance of the true velocities is given by

$$F_i = \frac{1}{N-i} \sum_{j=0}^{N-1-i} u'_{rj} u'_{ri+j} , \qquad (24)$$

so that the variance of the true velocities is obtained from the zeroth lag of equation (24), i.e., $\sigma_{u_r}^2 = F_0$. Although F_i cannot be computed directly from the data, it is possible to relate F_i to $\hat{F}_i$. Substituting equation (21) into (23) gives
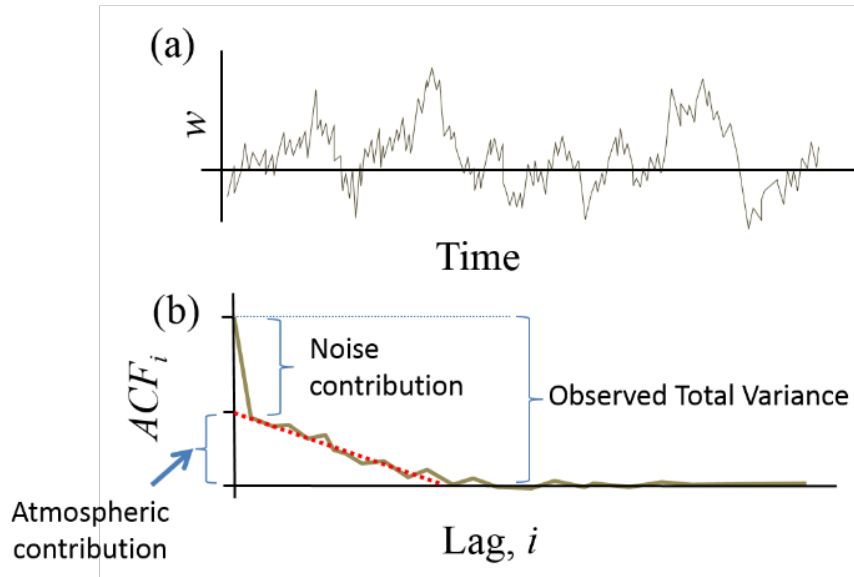
$$\hat{F}_i = \delta_{i0} \sigma_n^2 + F_i \qquad (25)$$

where δ_{i0} is the Kronecker delta function, which is 1 only when i=0. From (25) we see that

$$\hat{F}_i = F_i \text{ for } i > 0 .$$

This suggests that we can use $\hat{F}_i$ to estimate the true variance $\sigma_{u_r}^2$ by extrapolating $\hat{F}_i$ for i>0 to i=0, since $\sigma_{u_r}^2 = F_0$ (Lenschow et al. 2000, Frehlich 2001, 2004, Pearson et al. 2009). This process is illustrated in Figure 20. In this figure, the first few (nonzero) lags of the

autocovariance are used to extrapolate to zeroth lag. This then gives an estimate of the true atmospheric variance, $\sigma_{u_r}^2$, which in turn determines the noise variance from $\sigma_n^2 = \sigma_{\hat{u}_r}^2 - \sigma_{u_r}^2$.
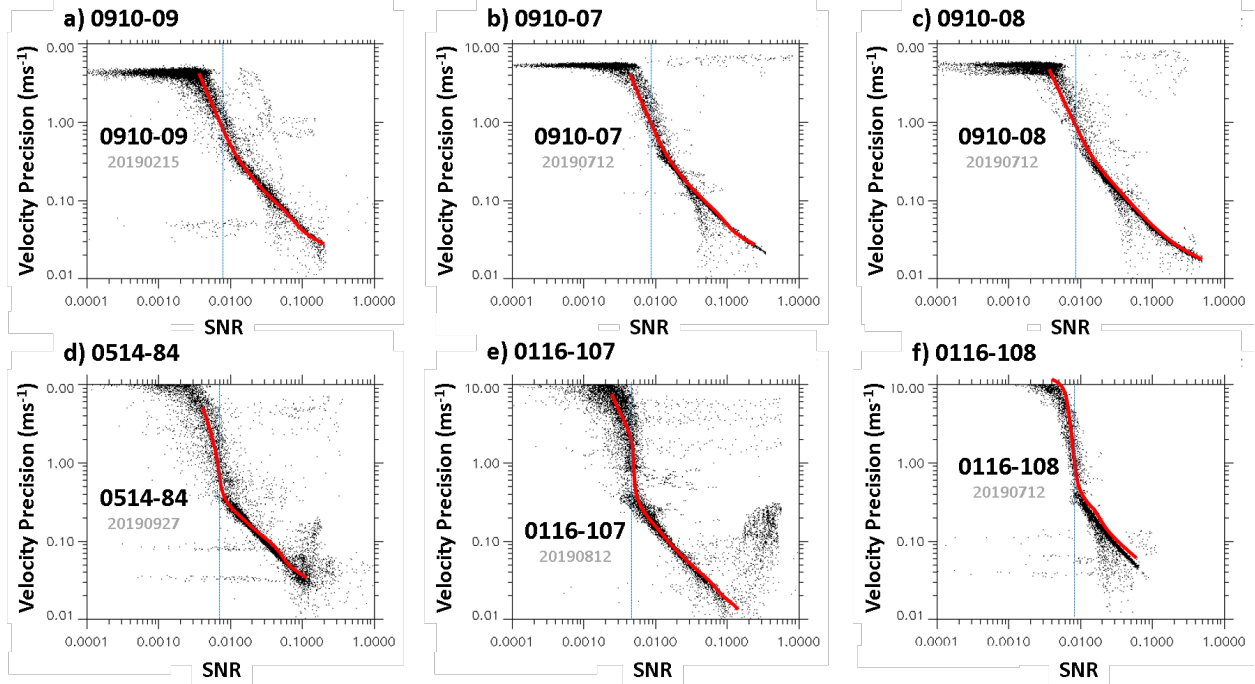
Figure 20. Method of estimating the true variance from the autocovariance of the observed velocity time series. Panel a) shows the observed time series, and panel b) shows the corresponding autocovariance. Noise in data manifests itself as spike at zeroth lag. The true variance is estimated by extrapolating the autocovariance from i>0 to i=0.

The analysis described above is typically done using a 30-min averaging period. The average SNR for each range is also computed, which then enables us to relate velocity precision to SNR. We note that the precision estimates are somewhat sensitive to the extrapolation method. There are a couple of ways of doing the extrapolation, and these are described in the following two subsections.

5.4.1   Linear Extrapolation

The simplest way of extrapolating the autocovariance is by fitting a straight line to the first few (nonzero) lags of the autocovariance. This is the procedure used in the ARM Doppler Lidar Vertical Velocity Statistics VAP (DLWSTATS, Newsom et al. 2019b). Currently, the DLWSTATS VAP uses a 30-minute interval to compute the autocovariance. It fits a straight line to lags 1 through 5 so that the y-intercept gives an estimate for the true atmospheric variance. Figure 21 shows examples of velocity precision as functions of mean SNR for several of the ARM Doppler lidars. The precision estimates in Figure 21 were obtained using the linear extrapolation method.

Figure 21. Estimates of radial velocity precision as functions of SNR for a) 0910-09, b) 0910-07, c) 0910-08, d) 0514-84, e) 0116-107, and f) 0116-108. The red curves are fits to the data. The blue vertical line indicates the SNR where the velocity precision is approximately 1 ms^{-1}.

5.4.2   Model-Based Extrapolation
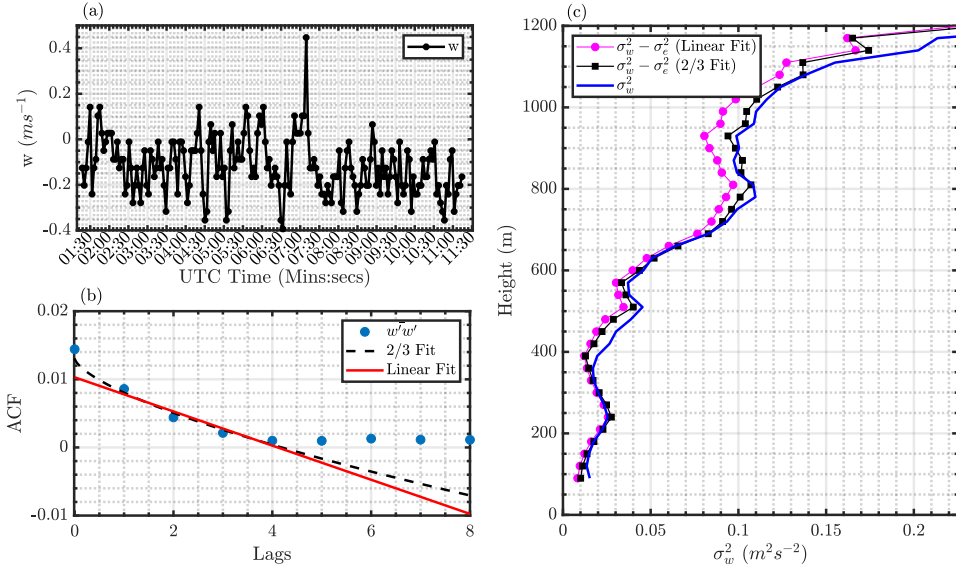
The inertial subrange hypothesis of homogeneous and isotropic turbulence (Monin and Yaglom 1979) implies an autocovariance function of the form (Lenschow et al. 2000)

$$F_{ij}^* = \overline{u_{rij}'^2} - \alpha \tau_i^{2/3} \tag{26}$$

where i is the lag index, j is the range index, α is an unknown parameter associated with turbulence eddy dissipation rate, u_{rij}' is the radial velocity fluctuation, and τ is the time-lag. By fitting equation 26 to the observed autocovariance, the true atmospheric velocity variance and the noise variance can be estimated. An estimate of the velocity precision is given by the difference between the model estimate and the observed autocovariance at zero lag, i.e.,

$$n_j \approx \sqrt{F_{0j} - F_{0j}^*} \tag{27}$$

Figure 22 shows a comparison between velocity precision estimates using both the linear and the model-based extrapolation methods. In this case, lags 1 through 4 were used to fit the model to the observed autocovariance. As shown in the figure, the linear extrapolation method tends to produce smaller estimates of the noise variance compared to the model-based extrapolation method. The differences increase with altitude (or as the SNR decreases).

Figure 22. a) Sample 10-min time series of vertical velocity from DL at 90 m AGL, b) Autocovariance function for the sample data set and respective linear or 2/3 fit, c) Vertical velocity variance profiles with and without noise correction.
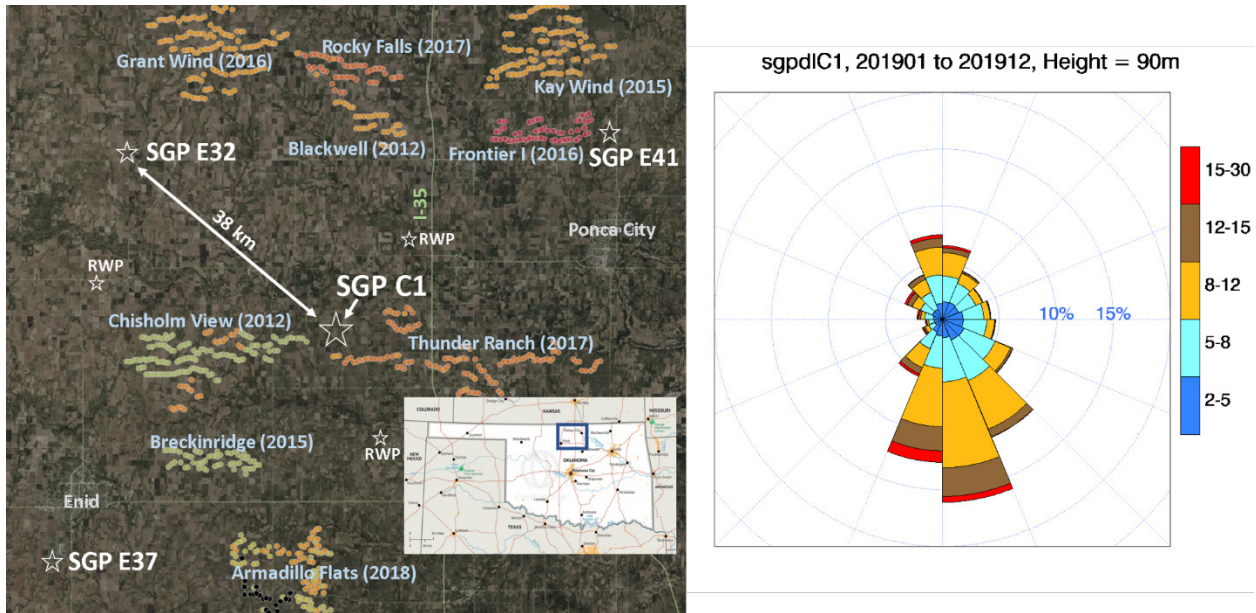
5.5 Beam Pointing Accuracy

Beam pointing accuracy impacts data quality (e.g., wind direction). The lidar reports the beam elevation and azimuth angles relative to the lidar's coordinate system. For ground-based systems, the ingest at the ARM Data Center (ADC) reads information from a configuration file in order to reference these angles to an Earth-fixed frame of reference. The configuration file, maintained by the instrument mentors, contains a history of the system's heading (i.e., the home point azimuth). The process of determining the orientation of the lidar is really a calibration issue, which is discussed in Section 6.4.2.

5.6 Potential Wind Farm Impacts on SGP

From 2012 to 2020 the pace of wind farm development in the vicinity of the SGP site has been frantic. Given the proximity of some of these turbines to the SGP sites, we expect some impact on low-level wind measurements. These impacts will likely increase in the future with further wind farm development.

Figure 23 shows the current (as of 2020) distribution of wind turbines in the vicinity of SGP. Of particular concern is the effect of several turbines located roughly 3 km south of the SGP Central Facility (C1), since the prevailing wind direction at SGP C1 is southerly, as indicated in Figure 23.

Figure 23. Left: Locations of wind turbine relative to SGP. Right: Wind rose for all of 2019 at 90 m AGL as measured by the Doppler lidar at SGP C1.

6.0   Instrument Details

This section discusses the theory of operation, instrument specifications, instrument configuration, scanning strategies, heading calibration, beam pointing accuracy, and calibration of the attenuated backscatter.

## 6.1   Theory of Operation

The ARM Doppler lidars employ a monostatic design, in which pulses of highly columnated laser radiation are transmitted into the atmosphere. The laser operates at the near-IR wavelength of $\lambda_o =$ 1548 nm. As the radiation propagates through the atmosphere it is scattered by aerosol and cloud particles (molecular scattering is very weak in the IR). Backscattered radiation is collected by the transceiver and processed to generate range-resolved estimates of radial velocity, attenuated backscatter and SNR. In general, the backscattered radiation experiences a Doppler shift that depends on the line-of-sight (radial) velocity of the scatterers relative to the lidar. A "red" shift occurs if the scatterers are moving away from the lidar, and a "blue" shift occurs if the scatterers are moving toward the lidar.

The Doppler shift of the backscattered radiation is quite small relative to the frequency of the outgoing pulse. As an example, a wind velocity of 30 ms^{-1} would result in a Doppler shift of only 10 MHz at 1548 nm. This amounts to a shift of 50 ppb relative to the optical frequency of 200 THz. Although tiny, it is possible to measure such small shifts with very good precision using coherent detection. The backscattered radiation from the atmosphere is mixed with light from a frequency-stable continuous-wave laser, i.e., the so-called local oscillator (LO). The mixed signal exhibits a modulation in the amplitude that oscillates at the frequency difference between the two beams. This is the signal that is detected, and the

modulation frequency indicates the Doppler shift (Grund et al. 2001, Rye and Hardesty 1993a,1993b, Frehlich 1999, Werner 2005).

As an example, consider a simplified case in which the electric field of the backscatter from the atmosphere can be modeled as a simple monochromatic plane wave, i.e.,

$$E_a = A_a e^{i(\omega_a t + \phi_a)} , \tag{28}$$

where A_a is the amplitude, ω_a is the angular frequency, t is time, and ϕ_a is an arbitrary phase. The frequency ω_a can be written as

$$\omega_a = \omega_o + \delta\omega_D \tag{29}$$

where ω_o is the frequency of the outgoing pulse, and $\delta\omega_D$ is a small ($\left|\delta\omega_D\right| << \omega_o$) Doppler shift due to scattering from moving aerosol. We note that $\delta\omega_D$ can be either positive for "blue" shifts or negative for "red" shifts. In this analysis, the frequency of the outgoing pulse, ω_o, is known; whereas the Doppler shift, $\delta\omega_D$, is to be determined.

The electric field for the local oscillator is also modeled as a monochromatic plane wave,

$$E_{LO} = A_{LO} e^{i(\omega_{LO} t + \phi_{LO})} , \tag{30}$$

where ω_{LO} is the LO frequency, which is also known.

In coherent detection the backscattered light from the atmosphere and the LO are superimposed by optically mixing and co-propagating the beams inside the transceiver. The combined beam is then directed onto a photodetector, which generates a signal in response the irradiance. For the current example, the irradiance at the photodetector is given by

$$I \propto \left|E_a + E_{LO}\right|^2 = A^2 + A_{LO}^2 + AA_{LO}\cos(\Delta\omega t + \Delta\phi) , \tag{31}$$

where

$$\Delta\phi = \phi - \phi_{LO} , \tag{32}$$

$$\Delta\omega = \omega_a - \omega_{LO} = \delta\omega_D + \Delta\omega_{offset} , \tag{33}$$

and

$$\Delta\omega_{offset} = \omega_o - \omega_{LO} \tag{34}$$

is the frequency offset between the outgoing pulse and the LO. In this example we assumed that the outgoing pulse is shifted up in frequency relative to the LO such that $\Delta\omega_{offset}$ is strictly positive.

Figure 24 shows the relationship between $\delta\omega_D$, $\Delta\omega_{offset}$, and $\omega_{Nyquist}$. The offset frequency is typically chosen to be half the Nyquist frequency, so that it lies in the center of the passband. This then enables retrieval of Doppler shifts in the range $\pm\omega_{Nyquist}/2$.

The DC terms in equation (31) are removed in signal processing so the detected signal in our simple example is essentially
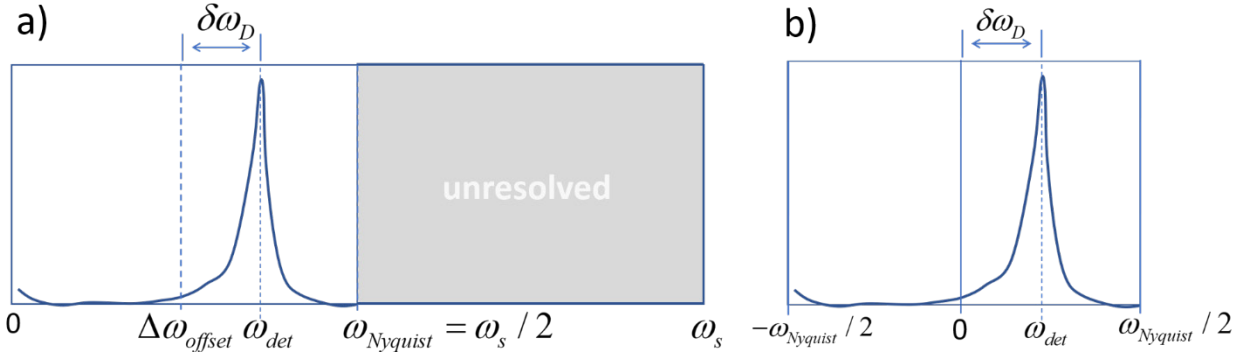
$$s(t) = \cos(\Delta\omega t + \Delta\phi)$$

(35)

In practice the detected signal contains the DC offset plus contributions from shot noise, detector relative intensity noise, and $1/f$ noise. The power spectrum of equation (35) yields a delta function centered at $\omega_{det} = \Delta\omega$, where ω_{det} is the frequency of the detected maximum in the power spectrum, as indicated in Figure 24. The Doppler shift is determined from

$$\delta\omega_D = \omega_{det} - \Delta\omega_{offset}$$

Figure 24a shows the relationship between $\delta\omega_D$, ω_{det}, $\Delta\omega_{offset}$, and $\omega_{Nyquist}$. The frequency of the outgoing pulse is chosen such that $\Delta\omega_{offset} \approx \omega_{Nyquist}/2$, i.e., in the center of the passband. This enables detection of Doppler shifts in the range of $\pm\omega_{Nyquist}/2$.

Figure 24. a) An example of an unshifted Doppler power spectrum, and b) the same spectrum after shifting to baseband, i.e., complex demodulation. In this example, ω_{det} denotes the angular frequency of the Doppler peak, which is of course different depending on which space you work in. In unshifted case (panel a) ω_{det} can range from 0 to $\omega_{Nyquist}$. In shifted case (panel b) ω_{det} can range from $-\omega_{Nyquist}/2$ to $\omega_{Nyquist}/2$.

In practice, complex demodulation is used to shift the spectrum of the signal to baseband. The demodulated signal is produced by splitting the received backscattered signal into two signals, mixing one

signal with a reference LO signal, and mixing the other signal with a 90° phase-delayed copy of the LO. This operation shifts the center of the passband to zero frequency, as indicated in Figure 24b. The result of the complex demodulation is given by

$$f(t) = e^{-i\omega_{offset}t} s(t) \tag{36}$$

The spectrum of the shifted signal is then given by

$$F(\omega) = S(\omega - \omega_{offset}), \tag{37}$$

where $S(\omega)$ is the Fourier transform of $s(t)$. In this case, the frequency of the Doppler peak gives the Doppler shift directly, i.e., $\omega_{\det} = \delta\omega_D$.

Traditionally, equation (36) is expressed in the following form

$$f(t) = I(t) + iQ(t) \tag{38}$$

where I and Q are referred to as the in-phase and quadrature signals, respectively. Equation (36) or (38) represent the baseband signal from a single laser shot.

In lidar, Doppler power spectra or its time-domain equivalent, the autocovariance function, must be computed for each laser shot and then averaged over a prescribed pulse integration time, which is typically around 1 sec or so. We note that this differs from the conventional approach in Doppler radar in which the power spectra are obtained from a time series of I&Q samples taken over multiple pulses. This approach fails for lidar because the detected signal from a given range is completely uncorrelated from one laser pulse to the next. This occurs because the displacements of the scatterers between pulses are generally much larger than the wavelength (Grund et al. 2001, Gossard and Strauch 1983).

The Halo Doppler lidars store spectral information in the form of autocovariance functions. Various terms of autocovariance matrix of the ungated signal, i.e., equation 38, are computed on a shot-by-shot basis and then averaged over the pulse integration period. At the end of the pulse integration period the truncated autocovariance functions for each range gate are computed, and then Fourier transformed to yield the gated Doppler power spectra, as described in Section 4.2.1. This approach takes advantage of the fact that the ACF and the power spectral density are Fourier transform pairs.

Once the Doppler frequency shift is determined, it is converted to a radial velocity using

$$u_r = -\frac{\lambda_o \delta\omega_D}{4\pi}, \tag{39}$$

where $\lambda_o = 1.548$ μm is the wavelength of the outgoing pulse. It is important to recognize that the radial velocity represents the radial component of the scatterer's velocity relative to the lidar. The negative sign in equation (39) implies that a negative Doppler shift (red shift) results in a positive radial velocity. We note that negative shifts occur when scatterers are moving away from the lidar. This would correspond to a case in which the radial distance between the lidar and the scatterer increases with time, which by definition is a positive velocity. Thus, all the ARM Doppler lidars report positive radial velocity for motion away from the lidar, and negative for motion towards the lidar.

We should note that all lidars are also susceptible to range ambiguities from clouds and other distant targets with large backscatter. The Stream Line and Stream Line Pro systems operate with a pulse repetition frequency of 15 kHz, which results in a maximum unambiguous range (MUR) of 10 km. The Stream Line XR and XR+ models operate at 10 kHz, giving an MUR of 15 km. Targets beyond the MUR can erroneously appear at closer ranges if there is sufficient backscatter. However, under normal operating conditions, the return signal beyond the MUR is usually quite weak, so that range ambiguity effects are quite small.

6.2   Specifications
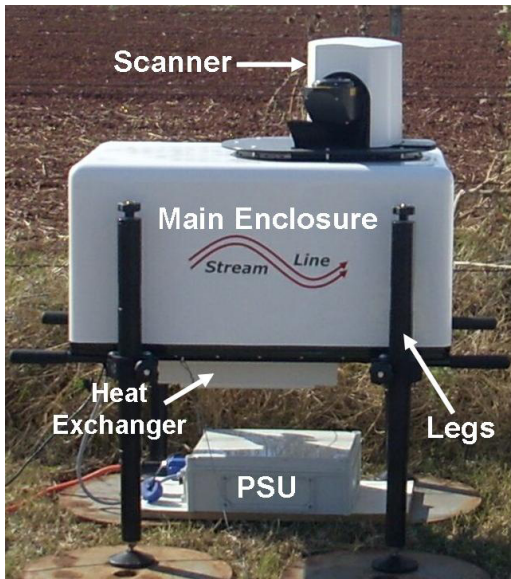
Performance specification of the ARM Doppler lidars are presented in Table 27. These instruments employ an eye-safe solid-state laser transmitter operating at a wavelength of 1.548 μm. The design incorporates all fiber-coupled components and uses a master oscillator power amplifier architecture (MOPA) for the generation of coherent light with low pulse energy (<100 μJ) and high pulse repetition frequency (15kHz). The Stream Line and Stream Line XR systems have full upper hemispherical scanning capability, while the Stream Line Pro systems use an internal scanner that only permits scanning to within ±20º from zenith. All systems provide range-resolved measurements of attenuated aerosol backscatter, radial velocity, and SNR. Control over the Doppler lidar is facilitated through a connection to the onboard computer. The onboard instrument control software allows the operator to adjust many system parameters and set up various scans. Further information about these systems and earlier versions can be obtained from Pearson et al. 2002, 2009, Davies et al. 2004, and Manninen et al. 2016.

Table 27.   Specifications of the ARM Doppler lidars.

	Stream Line Pro	Stream Line	XR, XR+
Eye safety	Class 1M		
Wavelength (μm)	1.5		
Laser pulse energy (μJ)	<100		
Aperture (mm)	50	75	75
Max data acquisition range (km)	9.6	9.6	12
Nyquist velocity (ms^{-1})	19.4		
Laser pulse width	~150 ns (22.5 m)		
Pulse rate (kHz)	15	15	10
Minimum range (m)	~50	~90	~90
Power consumption (W)	< 300		
Volume (m^3)	~ 1		
Mass (kg)	~ 85		
Temporal resolution (sec)	0.1 to 30		
Range gate size (m)	18 to 60		
Scanning	±20º from zenith	Upper hemisphere+	Upper hemisphere+
Enclosure	Weatherproof, temperature stabilized		

The major components of the ARM Doppler lidars are the main enclosure, the scanner, the heat exchanger, telescoping legs, and the power supply unit (PSU), as shown in Figure 25. The main enclosure houses all the transceiver optics and the onboard computer. As far as ARM is concerned, the main enclosure/scanner/heat exchange combination is regarded as a single unit. If any subcomponent within this unit fails, the entire unit must be sent back to the vendor for servicing.

The Stream Line and XR systems both use external scanners capable of steering the beam anywhere within the upper hemisphere. The Stream Line Pro, on the other hand, uses an internal scanner that can steer the beam anywhere within ±20° from zenith. Specific scans can be programmed to execute in a repeating manner or at specific times of day. The scan scheduling software allows one to set up both standard scan types (i.e., PPI, RHI, stare) or user-defined scans, e.g., a Lissajous figure in the sky. Additionally, there are two types of scan modes: step-stare and continuous motion. In step-stare mode the scan controller reads from a list of azimuth and elevation waypoints. The scanner stops momentarily at each waypoint and acquires data for a predefined pulse integration time. For continuous motion scans, the scanner moves continuously as data are acquired.


Figure 25. Components of the ARM Doppler lidar.

6.3 System Configuration and Scan Strategies

The instrument control software allows the operator to adjust settings that control measurement resolution, range resolution, and the temporal resolution of the output data. Additionally, the operator can program the system to execute specific scans on a regular repeating basis or at specific times of the day. Table 28 lists typical settings used by the ARM Doppler lidars. The range gate size is set to 30 m (10 raw samples) on most systems with the exception of the Stream Line Pro systems operating at NSA and Oliktok Point. For these systems a shorter range gate of either 18 or 24 m is typically used. Additionally, the pulse integration time for most staring data (i.e., scan type = fpt) is about 1 s, which is equivalent to a 15000 pulse average for the SL and Pro systems, and 10000 pulse average for the XR and XR+ systems. Table 28 lists typical values used to date.

Table 28.   Typical system settings used in the operation of the ARM Doppler lidars.

Raw samples per gate	6, 8, 10
Range gate size (m)	18, 24, 30
Number of pulses averaged per profile	15000, 30000
Pulse integration time (s)	1, 2
Points in FFT	1024

The standard scan schedule employed by most of the ARM systems involves primarily vertical stares and PPI scans. The vertical staring data are used to compute turbulence and cloud statistics (Newsom et al. 2019b). Once every 10 or 15 minutes, the lidars execute a single-pass step-stare PPI, from which profiles of wind speed and direction are computed (Newsom et al. 2019a). These PPI scans are performed at an elevation of 60°, using eight beams that are evenly spaced in azimuth from 0 to 360°. It typically takes about 40 seconds to complete one of these PPI scans. All systems are programmed to stare vertically when not performing any other scan type.

There are, however, periods and entire campaigns in which we deviate from the scan schedule described above. During the Surface Atmosphere Integrated Field Laboratory (SAIL) campaign twice-hourly RHI scans were added to the scan schedule. Also, at SGP there have been periods when we run two Doppler lidars in what we refer to as dual-mode operation.

6.4   Dual-Mode Operation

There have been a few periods over the years when spare (or brand new) systems become available at the SGP Central Facility that gave us the opportunity to run two systems together in some type of cooperative manner or dual-mode operation. When operating an additional Doppler lidar system at SGP C1, the facility name for the extra system is S01. Table 29 lists periods of dual-mode operation. Perhaps the simplest and most useful dual-mode operation is when the two systems are collocated, with one system performing PPI scans continuously, and the other system staring vertically without interruption. This mode enables the retrieval of all three components of the wind field with high temporal resolution. Estimates of total kinetic energy (TKE) can then be obtained from the results.

Table 29.   Periods with two Doppler lidars operating at the SGP Central Facility. The table lists the start and end times as well as the serial numbers and scan types associated with each facility name. The "wStare" scan is a vertical stare.

Dual-mode periods		C1		S01	
Start	End	s/n	scans	s/n	scans
20211117	20220123	0116-107	PPI	0710-08	wStare
20200930	20210108	0116-107	PPI	0720-193	wStare
20150723	20160408	0910-07	wStare, PPI	0710-08	wStare, PPI

6.5   Calibration

In this section we discuss the calibration requirements of the ARM Doppler lidars. This includes a discussion of the attenuated backscatter calibration, and the process of establishing and maintaining the correct heading relative to true north. We note that radial velocities require no calibration.

6.5.1   Attenuated Backscatter Calibration
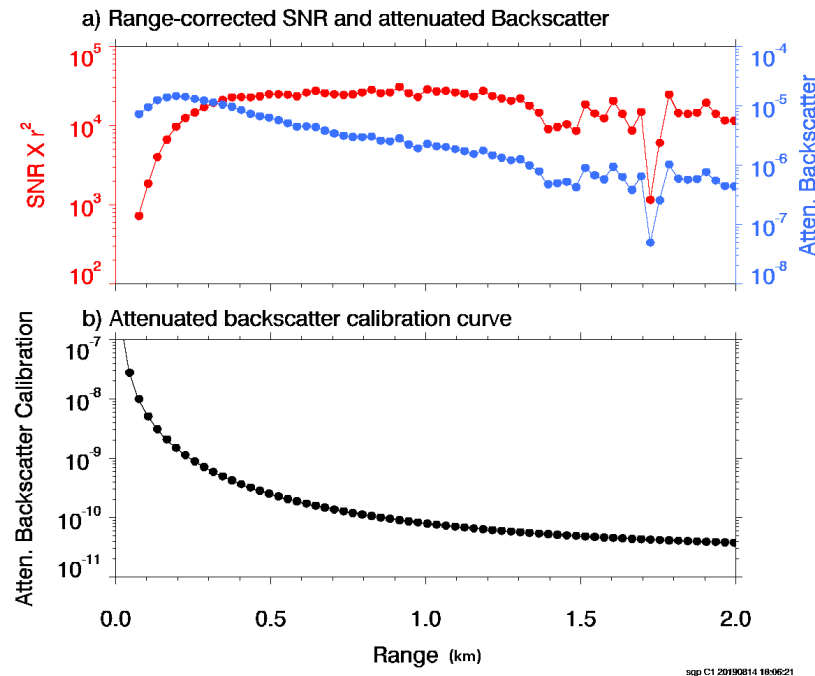
Attenuated backscatter measurements are derived the from the range-corrected SNR using a factory-determined calibration curve, i.e.,

$$\beta(r) = C(r)r^2 SNR(r) \tag{40}$$
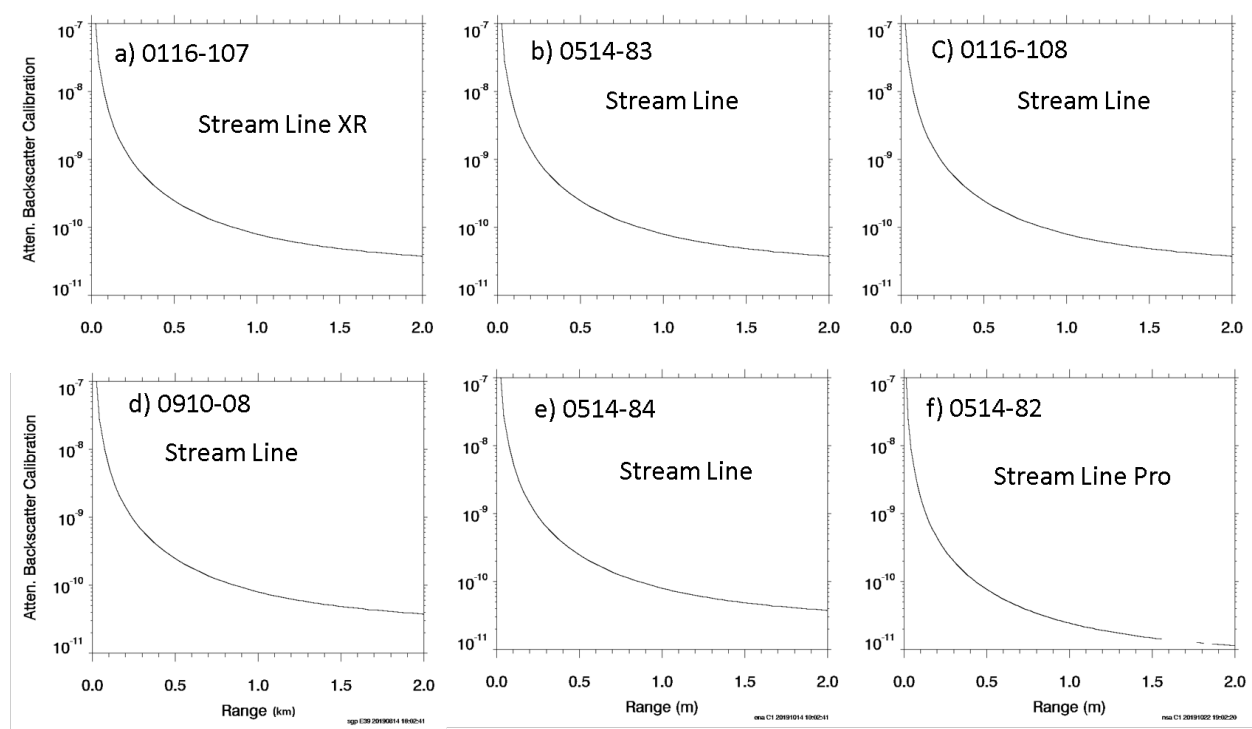
where $C(r)$ is the attenuated backscatter calibration curve, and $\beta(r)$ is the attenuated backscatter.

Figure 26 shows examples of attenuated backscatter, range-squared-corrected SNR, and the factory calibration curve for the 0116-107 system (Stream Line XR) at SGP C1 on 14 August 2019 at about 16:06 UTC.

To illustrate calibration differences between systems, Figure 27 shows calibration curves for several of the ARM DLs. The calibration curves for the Stream Lines and the XR are all quite similar but they are not identical, as there are small differences between them. By contrast, the calibration curve for the Stream Line Pro (i.e., the NSA system) is noticeably different.


Figure 26. a) range-corrected SNR (red) and attenuated backscatter (blue), and c) attenuated backscatter calibration curve. This example was obtained from the 0116-107 system (XR) at SGP C1 on 14 August 2019 at about 16:06 UTC.

Figure 27. Attenuated backscatter factory calibration curves for six of the ARM DLs.
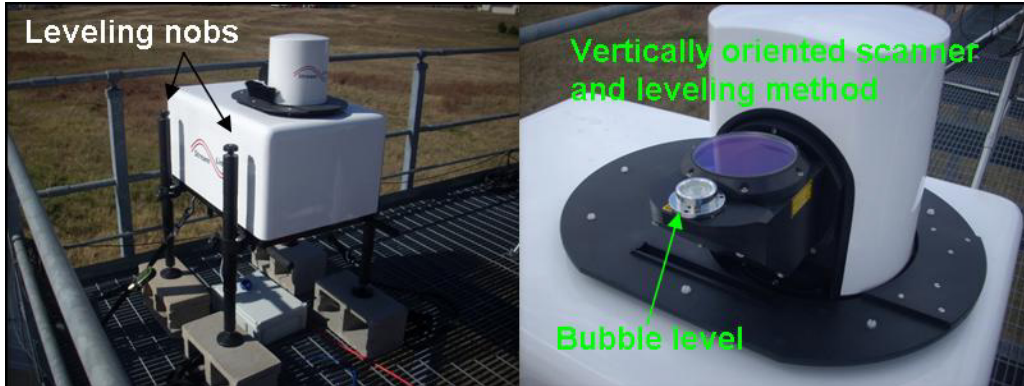
6.5.2   Heading Calibration

The lidar reports the beam azimuth and elevation angle relative to its own internal coordinate system. These angles are then transformed to an Earth-fixed frame of reference such that the azimuth is measured clockwise from true north, and the elevation angle is measured from the horizon. The process of establishing the orientation is different for ground-based and ship-based deployments, as well as for full scanning (e.g., Stream Line and XR) versus limited scanning systems (e.g., Stream Line Pro).

6.5.2.1   Ground-Based Deployments

The first step in establishing the lidar's heading is to ensure that the system is level. The levelness of all the ARM DLs systems is routinely monitored and adjusted (if necessary) by onsite technicians. Over the years, we have used two different leveling procedures. Originally, the level was determined by placing a small circular level on the scanner plate, and adjusting the leg heights accordingly, as shown in Figure 28. This method was used to level all the ground-based DLs from 2010 until late 2020. There is, however, no guarantee that the scanner plate is normal to the outgoing beam.
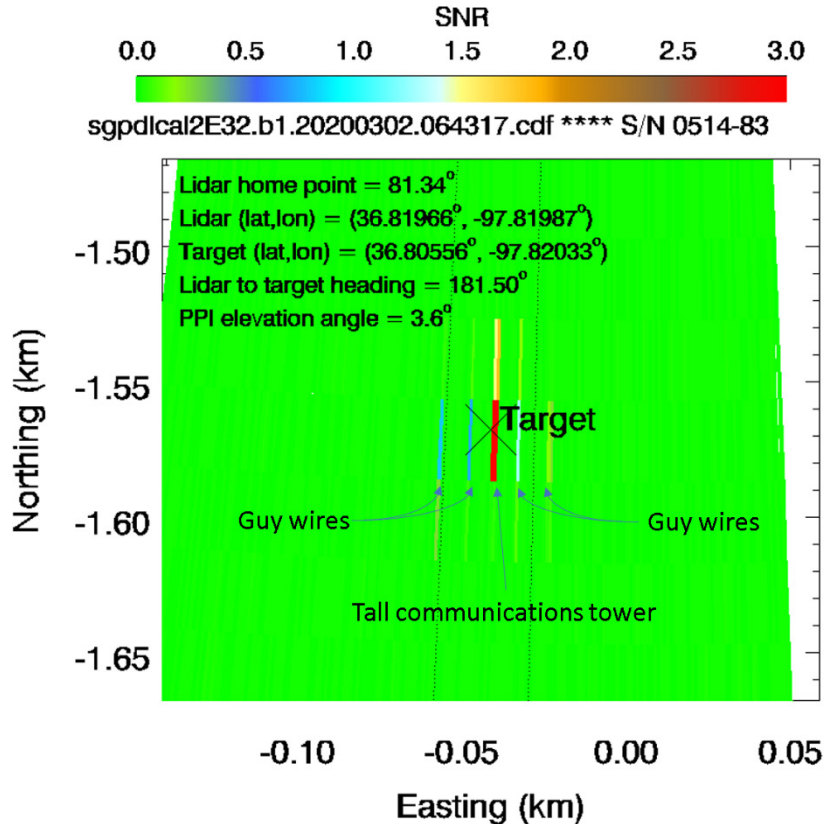
The preferred procedure is to level the lidar based on measurements for its internal tilt sensor. The tilt sensor provides measurements of pitch and roll, which are displayed in real time by the instrument control program. In December 2020, we transitioned to using the tilt sensor measurements for leveling the lidars.
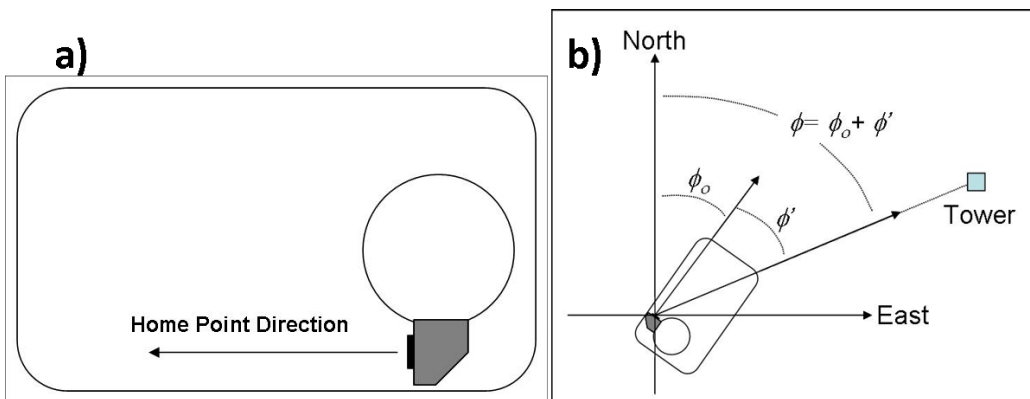
Figure 28. The old procedure for leveling involves placing a small circular level on the scanner plate while the scanner is in a vertical position. Leveling nobs on the legs are used to adjust the leg heights.

The method for determining the heading depends on whether the system has a full upper hemispheric scanner. In the case of the Stream Line Pro, which does not have a full upper hemispheric scanner, an arrow on the top of the unit indicates north. The alignment process simply involves manually aligning the lidar so that the arrow points towards true north. This is typically done using a handheld Global Positioning System (GPS) compass or smart phone while accounting for the local magnetic declination.

For the ground-based Stream Line and Stream Line XR systems, we use the full scanning capability to establish the lidar's heading, or home point. The home point is the true azimuth (as measured clockwise from true north) of the beam when the azimuth reported by the lidar is zero. The scanner position of the home point is indicated in Figure 30. The procedure used for establishing the home point involves performing a low-elevation sector scan in the general direction of a narrow, isolated feature (target) that pokes above the horizon and that lies roughly 200 to 2000 m from the lidar. Possible targets include power poles, light poles, cell phone towers, radio towers, meteorological towers, etc. Figure 29 shows an example of one such scan that was performed by the 0514-83 system at SGP E32 on 2 March 2020. In this case the target is a tall communications tower located approximate 1.55 km south of the lidar. The target's azimuth relative to the lidar's home point can be accurately determined from the location of the hard-target return in the intensity (SNR+1) or SNR field. The home point azimuth relative to true north can then be determined from the known GPS coordinates of the lidar and target, which are obtained from handheld GPS, smartphone, or Google Earth.

SNR

| 0.0 | 0.5 | 1.0 | 1.5 | 2.0 | 2.5 | 3.0 |

sgpdlcal2E32.b1.20200302.064317.cdf **** S/N 0514-83

Lidar home point = 81.34°
Lidar (lat,lon) = (36.81966°, -97.81987°)
Target (lat,lon) = (36.80556°, -97.82033°)
Lidar to target heading = 181.50°
PPI elevation angle = 3.6°

Target

Guy wires — — Guy wires

Tall communications tower

Northing (km)

Easting (km)

Figure 29. Example showing the SNR obtained from a hard-target scan. In this case, the target is a tall communications tower located approximately 1.55 km south of the lidar. Scans like this are performed on a once-per-day basis at all sites with full scanning capability, i.e., all sites with either a Stream Line or an XR.

a)

Home Point Direction

b) North

$\phi = \phi_o + \phi'$

ϕ_o

ϕ'

Tower

East

Figure 30. a) Schematic top view of the Stream Line and/or XR lidar with the scanner in its home position, and b) the geometry for determining the home point direction of the lidar. The azimuth of the home point relative to true north is ϕ_o, and the relative azimuth to the target, as determined from the lidar scan data, is ϕ'. In this example, the tower provides a reference hard-target return for the lidar. The home point azimuth can be determined if accurate GPS measurements of the lidar and the tower are known.

6.5.2.2   Ship-Based Deployments

To date, the only ship-based deployment of an ARM Doppler lidar has been during the MOSAiC field campaign. During that campaign a Stream Line Pro (serial number 0319-160) was deployed aboard the German icebreaker *Polarstern*. The information necessary to correct for platform motion was obtained from the ARM Navigational Location and Attitude (NAV) system (Walton 2019), and the lidar's internal tilt sensor.

During MOSAiC the north arrow on the top of the Stream Line Pro was aligned with the stern-to-bow line, and thus coaligned with the heading axis of the NAVsystem. In order to use the NAV data to describe the lidar's attitude and velocity, the pitch and roll offsets and the displacement between the lidar and the NAV must be known. The pitch and roll offsets were determined by comparing data from the lidar's internal tilt sensor to the NAV pitch/roll data. The components of the displacement vector between the NAV gyros and the lidar were also measured. The NAV data, together with the pitch/roll offsets and the NAV-to-lidar displacement vector, were then used to transform the beam angles from the lidar's frame of reference to an Earth-fixed frame of reference, and to correct the radial velocity measurements for translational motion (surge, sway, heave) of the lidar.

One of the shortcomings of this approach is the uncertainty in the lidar's heading axis, since this is determined completely by eye. For future ship-based deployments we plan to add an external inertial measurement unit (IMU) to the lidar. This will eliminate the reliance on the NAV system, and should reduce the uncertainty associated with the lidar's heading direction.

6.5.2.3   Flip Test

In general, there is a small offset between the reported beam direction and the true beam direction, as illustrated in Figure 31. If not compensated for, the effect of these offsets can be significant, particularly in applications requiring highly precise pointing accuracy, e.g., dual Doppler.

One method used for determining the beam direction offset is the so-called "flip test." The idea behind the flip test is that the beam pointing direction should be unaffected by rotating the scanner from (az, el) to (az+180°,180°-el). In practice, the beam is seldom perfectly aligned with the scanner boresight, so the beam direction will change slightly as a result of the rotation.

To determine the azimuth offset we perform a sequence of two high-resolution low-elevation PPI sector scans in the direction of a narrow isolated feature such as a power pole. For the first scan, which we call the non-flipped scan, the elevation angle is less than 90°. For the second scan, i.e., the flipped scan, the azimuth and elevation angles are defined such that

$$az_{flip} = az + 180°$$

(41)

and

$$el_{flip} = 180° - el,$$

(42)

where az and el are the azimuth and elevation angles from the non-flipped scan. When analyzing these scans, the target returns will, in general, be shifted slightly in azimuth, as illustrated in Figure 32a. The azimuth offset is determined from

$$\Delta az = \frac{1}{2}\left(az' - az'_{flip}\right),$$

(43)
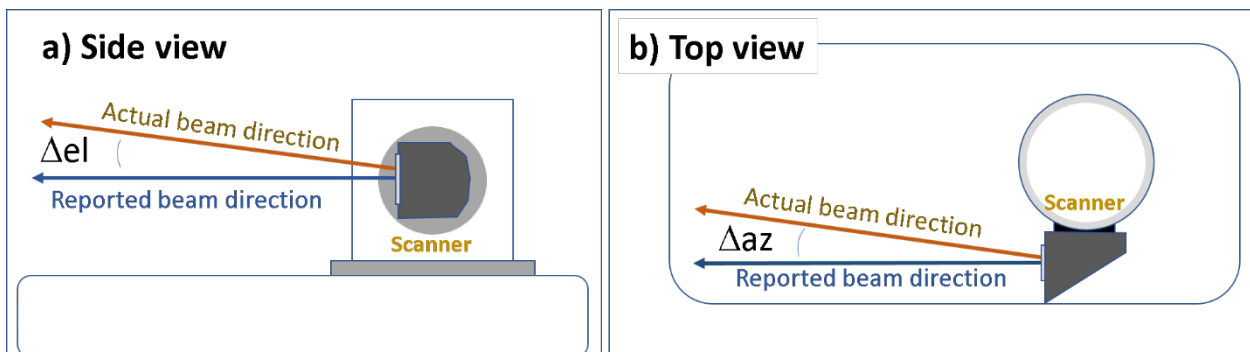
where az' and az'_{flip} are the azimuths of the target in the non-flipped and flipped scans, respectively.

To determine the elevation offset we perform a sequence of two (non-flipped and flipped) high-resolution RHI sector scans from the horizon to 2 or 3 degrees below the horizon. In this way, we use the ground return as our target. This approach works well at SGP where the terrain is flat and there are few trees to contend with. Also, all the SGP DLs are positioned approximately 3 m AGL on top of trailers, which provides a little better vantage point when scanning below the horizon. Figure 32b shows the apparent elevation angle of the ground return (at a range of ~500 m) in the flipped and non-flipped scans. The elevation offset is determined from
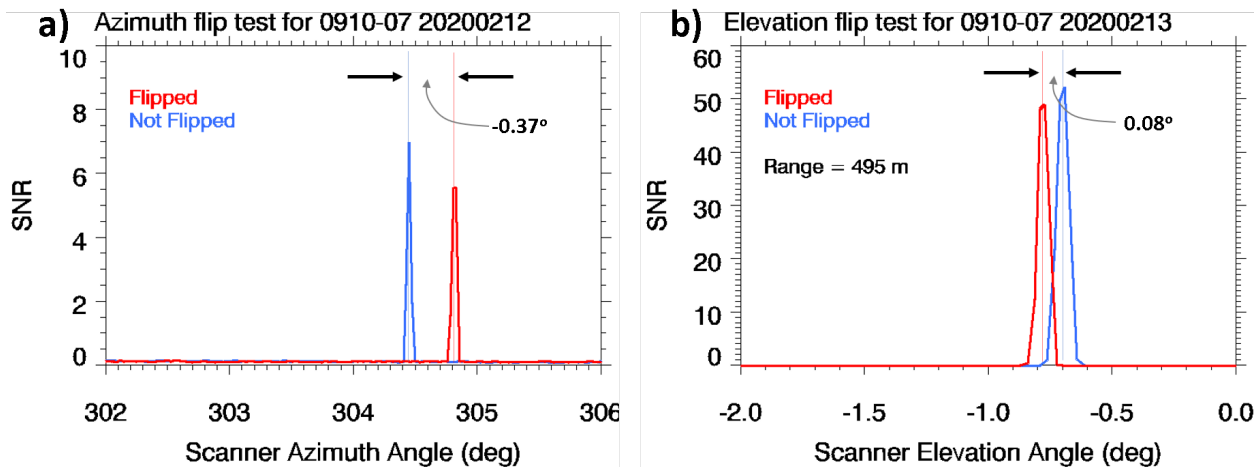
$$\Delta el = \frac{1}{2}\left(el' - el'_{flip}\right),$$

(44)

where el' and el'_{flip} are the elevation angles of the target in the non-flipped and flipped scans, respectively.

The results of a flip test performed on 0910-07 are shown in Figure 32. This test was done on 12 and 13 February 2020 when the 0910-07 was deployed at SGP E41. The results indicate an azimuth offset of $\Delta az = -0.19°$, and an elevation offset of $\Delta el = +0.04°$. Thus, in order to correct the data for beam misalignment, one should add these offsets to the azimuth and elevations angles reported by the 0910-07 system. We note that these corrections are not currently applied to any of the ARM Doppler lidars. In the future, we plan to repeat this analysis for all the ARM scanning DLs.


Figure 31. a) side view, and b) top view of the Halo Stream Line lidar illustrating a hypothetical offset between the reported beam direction and the actual beam direction. The purpose of the flip test is to determine the azimuth and elevation offsets, Δaz and Δel, respectively.

Figure 32. Flip test results for 0910-07 showing a) the azimuth offset, and b) the elevation offset. The blue and red curves show the target returns from the non-flipped and flipped scans, respectively. These results indicate that the actual beam is offset by -0.19º in azimuth and +0.04º in elevation for the 0910-07 system. This test was conducted on 12 and 13 February 2020 at SGP E41.

6.6   Operation and Maintenance

6.6.1   User Manual

The operations manual is considered proprietary by the vendor and is only made available to authorized personnel. Requests for information regarding the operation of the Doppler should be directed to the instrument mentor(s).

6.6.2   Routine and Corrective Maintenance Documentation

Routine and corrective maintenance documentation is maintained by onsite technicians and the instrument mentor(s).

7.0   References

ARM Standards Committee, 2016. ARM Data File Standards: Version 1.2. U.S. Department of Energy. DOE/SC-ARM-15-004.

Berg, LK, RK Newsom, and DD Turner. 2017. "Year-Long Vertical Velocity Statistics Derived from Doppler Lidar Data for the Continental Convective Boundary Layer." *Journal of Applied Meteorology and Climatology* 56(9): 2441–2454, https://doi.org/10.1175/JAMC-D-16-0359.1

Davies, F, CG Collier, GN Pearson, and KE Bozier. 2004. "Doppler Lidar Measurements of Turbulent Structure Function over an Urban Area." *Journal of Atmospheric and Oceanic Technology* 21(5): 753–761, https://doi.org/10.1175/1520-0426(2004)021<0753:DLMOTS>2.0.CO;2

Frehlich, RG. 2001. "Estimation of velocity error for Doppler lidar measurements." *Journal of Atmospheric and Oceanic Technology* 18(10): 1628−1639, https://doi.org/10.1175/1520-0426(2001)018<1628:EOVEFD>2.0.CO;2

Frehlich, R. 2004. "Velocity Error for Coherent Doppler Lidar with Pulse Accumulation." *Journal of Atmospheric and Oceanic Technology* 21(6): 905–920, https://doi.org/10.1175/JTECH1596

Frehlich, RG. 1999. "Performance of maximum likelihood estimators of mean power and Doppler velocity with a priori knowledge of spectral width." *Journal of Atmospheric and Oceanic Technology* 16(11): 1702−1709, https://doi.org/10.1175/1520-0426(1999)016<1702:POMLEO>2.0.CO;2

Gossard, EE, and RG Strauch. 1983. *Radar Observations of Clear Air and Clouds*. Elsevier, Amsterdam.

Grund, CJ, RM Banta, JL George, JN Howell, MJ Post, RA Richter, and AM Weickmann. 2001. "High-resolution Doppler lidar for boundary layer and cloud research." *Journal of Atmospheric and Oceanic Technology* 18(3): 376–393, https://doi.org.10.1175/1520-0426(2001)018<0376:HRDLFB>2.0.CO;2

Lenschow, DH, V Wulfmeyer, and C Senff. 2000. "Measuring Second- through Fourth-Order Moments in Noisy Data." *Journal of Atmospheric and Oceanic Technology* 17(10): 1330–1347, https://doi.org/10.1175/1520-0426(2000)017<1330:MSTFOM>2.0.CO;2

Manninen AJ, EJ O'Connor, V Vakkari, and T Petäjä. 2016. "A generalised background correction algorithm for a Halo Doppler lidar and its application to data from Finland." *Atmospheric Measurement Techniques* 9(2): 817−827, https://doi.org/10.5194/amt-9-817-2016

Monin, AS, and AM Yaglom. 1979. *Statistical Fluid Mechanics*. MIT Press, Cambridge, Massachusetts.

Newsom RK, C Sivaraman, TR Shippert, and LD Riihimaki. 2019a. Doppler Lidar Wind Value-Added Product. U.S. Department of Energy. DOE/SC-ARM/TR-148.

Newsom RK, C Sivaraman, TR Shippert, and LD Riihimaki. 2019b. Doppler Lidar Vertical Velocity Statistics Value-Added Product. U.S. Department of Energy. DOE/SC-ARM-TR-149.

Newsom R, W Brewer, J Wilczak, D Wolfe, S Oncley, and J Lundquist. 2017. "Validating precision estimates in horizontal wind measurements from a Doppler lidar." *Atmospheric Measurement Techniques* 10(3): 1229−1240, https://doi.org/10.5194/amt-10-1229-2017

Pearson, GN, PJ Roberts, JR Eacock, and M Harris. 2002. "Analysis of the performance of a coherent pulsed fiber lidar for aerosol backscatter applications." *Applied Optics* 41(30): 6442−6450, https://doi.org/10.1364/AO.41.006442

Pearson, GN, F Davies, and C Collier. 2009. "An analysis of the performance of the UFAM pulsed Doppler lidar for observing the boundary layer." *Journal of Atmospheric and Oceanic Technology* 26(2): 240−250, https://doi.org/10.1175/2008JTECHA1128.1

Rye, BJ, and RM Hardesty. 1993a. "Discrete spectral peak estimation in incoherent backscatter heterodyne lidar. I. Spectral accumulation and the Cramer-Rao lower bound." *IEEE Transactions on Geoscience and Remote Sensing* 31(1): 16−27, https://doi.org/10.1109/36.210440

Rye, BJ, and RM Hardesty. 1993b. "Discrete spectral peak estimation in incoherent backscatter heterodyne lidar. II. Correlogram accumulation." *IEEE Transactions on Geoscience and Remote Sensing* 31(1): 28–35, https://doi.org/10.1109/36.210441

Walton, SM. 2019. Navigational Location and Attitude (NAV) Instrument Handbook. U.S. Department of Energy. DOE/SC-ARM/TR-226.

Werner, C. 2005. "Doppler wind lidar." In *Lidar: Range-Resolved Optical Remote Sensing of the Atmosphere*. C Weitkamp, Ed. Series in Optical Sciences, 102, Springer, New York, pp. 325–354.

Appendix A

AET Raw Data Format

Raw data files from the ARM DLs are transferred from the instrument to the ADC and then converted from the original vendor format to netCDF following ARM data object design standards. In Section 4.2 we provided a detailed description of the contents of the netCDF files (i.e., the <site>dlacf<facility>.a0 datastream). In this section, we provide a detailed description of the original raw vendor format. We do this because this format has not been previously published, as far as we are aware.

Below we describe the format of the raw data that are generated when the "AET" option is selected in the 'System setup' tab of the instrument control program (i.e., the Stream Line vi). We refer to this as the AET format.

AET raw files are generated using "little endian" byte ordering, and all words are stored as 8-byte floats, i.e., double precision values. The number of lags in the ACF, nlags, and the number of I&Q samples per beam, nsamples, are system dependent. For the Stream Line XR, nlags = 20 lags and nsamples = 4000. For the Stream Line and Stream Line Pro, nlags = 7 lags and nsamples = 3200. The binary data in the AET raw data files are organized as follows:

- Noise background data (acquired hourly by the lidar and prepended to each raw file)
    - s_{j0}^{bkg} (real, imaginary) *j=0...nsamples-1* (2 x nsamples x 8 bytes)
    - ...
    - $s_{j,nlags-1}^{bkg}$ (real, imaginary) *j=0...nsamples-1* (2 x nsamples x 8 bytes)
- Beam data (repeated for as many beams as exist in the file)
    a. Azimuth angle in degrees (8 bytes)
    b. Elevation angle in degrees (8 bytes)
    c. Time stamp in decimal hours (8 bytes)
    d. s_{j0}^{atm} (real, imaginary) *j=0...nsamples-1* (2 x nsamples x 8 bytes)
    e. …
    f. $s_{j,nlags-1}^{atm}$ (real, imaginary) *j=0...nsamples-1* (2 x nsamples x 8 bytes)